applied optics

Transport of intensity and phase: applications to digital holography [Invited]

Nouf A. Alanazi,[1,2] Austin M. Scott,[1] Hammid Al-Ghezi,[1] Muhammad Faryad,[3] Akhlesh Lakhtakia,[3] and Partha P. Banerjee[1,*]

[1]Department of Electro-Optics and Photonics, University of Dayton, Dayton, Ohio 45469, USA
[2]Current address: Department of Physics, Imam Abdulrahman bin Faisal University, Dammam 34212, Saudi Arabia
[3]Department of Engineering Science and Mechanics, The Pennsylvania State University, University Park, Pennsylvania 16802, USA
*pbanerjee1@udayton.edu

Received 15 January 2024; revised 28 February 2024; accepted 29 February 2024; posted 1 March 2024; published 21 March 2024

We first review transport of intensity and phase and show their use as a convenient tool to directly determine the unwrapped phase of an imaged object, either through conventional imaging or using digital holography. For both cases, either the traditional transport of intensity and phase, or with a modification, viz., electrically controllable transport of intensity and phase, can be used. The use of digital holography with transport of intensity for 3D topographic mapping of fingermarks coated with columnar thin films is shown as an illustrative application of this versatile technique.

https://doi.org/10.1364/AO.519170

1. INTRODUCTION

The phase retrieval problem has a history spanning many decades [1] and manifests in numerous scientific disciplines including astronomy [2,3], electron microscopy [4,5], x-ray crystallography [6,7], and optical imaging [8–10]. As pointed out by Oppenheim and Lim [11], in the Fourier representation of signals, the phase content alone may contain most of the important information, and in many cases is enough to completely reconstruct the signal to within a scale factor. The measurement of phase began with Zernike [12] and Nomarski [13] for their respective inventions of the phase contrast and differential interference contrast microscopes, which were limited to only qualitative measurements. Advancements in computing capabilities and the use of digital image sensors [14] eventually led to quantitative phase imaging methods, which have had significant impacts in optical metrology [15–18] and biomedical imaging [19–21]. Quantitative phase measurement techniques fall into two distinct categories, namely, interferometric [22,23] and non-interferometric [24–27].

Digital holography (DH) is an interferometric technique of obtaining phase information whereby holograms are recorded on a CCD or CMOS detector and numerically reconstructed using a computer [28–30]. Allowing both 3D and quantitative phase images of objects to be recovered, DH has been successfully employed in non-destructive testing and metrology [31], microscopy [32,33], particle flow measurements in 3D space [34], 3D imaging of biological samples [35], 3D image encryption [36], 3D object recognition [37], 3D tomographic imaging [38], 3D surface shape measurement with nanometer depth sensitivity [39], ultrafast 3D optical imaging [40], and 3D imaging with a single-pixel detector [41,42]. Various system architectures exist for DH, such as phase-shifting DH [43–47] where the object and reference beams are nominally copropagating to the image sensor and multiple holograms are recorded with a phase shift applied to the reference beam between each recording, and off-axis DH [48–53] where a slight angle is introduced between the object and reference beams as they propagate to the image sensor. The off-axis setup allows separation of the object-wave information from the unwanted DC and twin image components by filtering in the spatial frequency domain or spatial separation after reconstruction. In the first case, after isolation of the object-wave information, a 2D inverse Fourier transform followed by numerical back propagation to the object plane recovers the complex amplitude and phase image of the object [22,28,54]. The phase image reconstructed from the digital hologram is a wrapped phase, meaning it must be unwrapped to obtain the true phase. This can be done using a phase unwrapping algorithm such as the phase unwrapping max-flow algorithm (PUMA) [55]. While other phase unwrapping algorithms exist [56,57], PUMA is chosen primarily by our group due to its speed and robustness.

The transport of intensity is a non-interferometric method for phase retrieval capable of recovering the true phase of an object without the need for phase unwrapping [24,58]. The transport of intensity equation (TIE) is derived from the Helmholtz equation under the paraxial approximation [59,60], and is a deterministic phase retrieval method requiring a minimum of two axially separated intensity images. Multiple intensity images are required to estimate the axial intensity derivative using finite difference methods, and much work has been done to improve the accuracy of the phase retrieval by improving the axial intensity derivative estimate. This has been done using higher-order intensity derivative estimates with equally spaced defocus planes [61,62], exponentially spaced defocus planes with Gaussian regression fitting of the axial intensity derivative [63], and simultaneous recording of defocused intensity images using volume holograms [64], which eliminates the need for any axial displacement of the image sensor or the object during recording. Other single-shot architectures for TIE-based phase imaging include using computer generated holograms (CGHs) at a Fourier plane of the object to generate defocused point spread functions [62], and tilted mirrors in a Michelson interferometer [65].

Banerjee *et al.* [66] derived the TIE independently along with the associated transport of phase equation (TPE), which are the imaginary and real parts of the paraxial wave equation, respectively. The imaginary part of the paraxial wave equation, or TIE, represents the conservation of energy for a propagating electromagnetic wave, while the real part, or TPE, is the eikonal equation in the presence of diffraction [67]. The complex amplitude and phase must satisfy both the real and imaginary parts of the paraxial wave equation simultaneously, and several numerical methods exist to find the solution. Among them are the fast Fourier transform (FFT) methods [68–70], discrete cosine transform (DCT) methods [71,72], matrix methods [73,74], and iterative methods such as the Gerchberg–Saxton algorithm [75], input-output approach [76], and the Jacobi iteration algorithm [77]. For a comparison of various iterative algorithms for phase retrieval from intensity images, the reader is referred to [78–80]. In 2016, Basunia *et al.* [81] demonstrated improvements in the phase retrieval through a recursive calculation of the phase and intensity using the TIE and TPE, respectively, with the TPE being solved each time using a Gauss–Seidel iterative method [82]. Zhang *et al.* [83] in 2017 showed that finite difference methods for solving the TIE provide better accuracy than traditional FFT-based methods at the cost of longer computation times. A non-recursive method incorporating the TPE as a correction factor to the TIE was introduced by Zhou and Banerjee [67,84], improving the accuracy of the phase retrieval while maintaining low computation times. Another approach to improve the accuracy of TIE-based phase retrieval is to reduce the experimental errors, a significant source of which can be the axial translation of the image sensor or object during recording of intensity images at multiple defocused planes, leading to transverse (x, y) displacements between the recorded intensities. Gupta *et al.* [85,86] proposed a method using electrooptic (EO) materials such as liquid crystals (LCs) to electrically control the optical path length (OPL) between the object and the image sensor, thereby requiring no physical movement. A similar approach was taken by Chen *et al.* [87], where an LC phase shifter was used to manipulate the refractive index through which the object wave propagates, and a new equation relating intensity and phase was derived with respect to the variation of refractive index. In 2022, a phase retrieval method using the modified TIE with the TPE [67] correction factor employing electrically controllable OPL was proposed, and the corresponding modified TPE was also derived and can be used to enhance the accuracy of the modified TIE [88].

Individually, DH and TIE are methods of obtaining quantitative phase information about a given sample, whether that is a phase image, 3D surface profile, or refractive index distribution, with each method having its own strengths and weaknesses. For example, DH is an interferometric method requiring (usually) coherent light sources and a separate (reference) wave to interfere with the object wave, resulting in speckle noise, increasing alignment difficulties and susceptibility to environmental noise. In addition, digital holograms provide wrapped phase information that must be unwrapped using phase unwrapping algorithms that can be computationally taxing. However, only a single recorded hologram is necessary to obtain full 3D complex phase and amplitude information [89–91]. The TIE approach, being non-interferometric, uses simpler experimental setups that are less sensitive to environmental noise, albeit at the cost of having to take numerous intensity images at various axial planes. Additionally, the TIE operates on several assumptions that may not always be satisfied in experimental conditions, and low intensity values at the image plane or poorly defined phase boundaries in the transverse dimension cause problems when solving the TIE [24,92]. There is much recent work in the *comparison* of DH and TIE methods for QPI, especially in microscopy and imaging of biological samples that present as phase objects, such as live cells [93–97].

In 2013, a novel approach for phase demodulation in 3D digital holographic imaging via *combination* of DH and TIE methods was proposed by Zuo *et al.* [98], providing a means to directly recover the true phase and depth information of an object from its recorded hologram while avoiding phase unwrapping problems. Memarzadeh *et al.* [99] combined the TIE with tomography to recover the true 3D shape of both stationary and moving phase and amplitude objects in 2014. It has also been shown that the TIE can be used to remove the quadratic phase aberration inherent in phase images retrieved using DH [100], solve the twin image problem in in-line holographic x-ray imaging [101], reduce the speckle noise in phase images extracted from off-axis digital holograms [102], improve the accuracy of phase retrieved from single-shot digital holograms for materials monitoring [103], and provide benefits to 3D polarization imaging [104]. In 2018, Zhou *et al.* [105] presented a method where multiple intensity images are reconstructed at different axial planes from a single digital hologram, and then those intensity images are used as the inputs to the TIE, from which the unwrapped phase is then recovered. With this approach, the TIE acts as a phase unwrapping algorithm for the DH-based phase retrieval, and the digital hologram reconstruction process allows the employment of the TIE without needing to physically translate any optics to record the multiple intensity images [106,107]. Recently, phase retrieval through off-axis DH with a modified TIE + TPE correction factor using electrooptic materials for electrically programmable optical path lengths was proposed [108]. The DH + TIE + TPE method, both with and without LCs, has been verified as an interferometric, deterministic phase retrieval technique that gives the unwrapped phase of the reconstructed object while eliminating the need for physical translation of the image sensor or object and has been utilized for recovering the 3D height profile of fingermarks coated with a columnar thin film (CTF) [109]. It should be noted that the use of the FFT-based TIE to recover the unwrapped phase from a digital hologram imposes the assumption of periodic boundary conditions onto the phase of the digital hologram. Since phase recovery using DH alone requires no specific boundary conditions, using the FFT-based TIE for unwrapping could cause phase-boundary artifacts in the recovered phase profile. One way to avoid this issue is to ensure that the intensity images used in the TIE go zero at the boundaries, either by cropping a larger area from the reconstructed intensity images or by zero-padding the intensity images before employing the TIE.

The rest of this manuscript is organized as follows. Section 2 begins with a brief derivation of the TIE, TPE, and the correction factor used to improve the phase retrieval when using the combined non-recursive TIE + TPE. Results of simulations comparing the performance of non-recursive TIE + TPE over TIE alone for phase retrieval are shown. Section 3 shows unwrapped phase retrieval from simulated off-axis digital holograms using TIE, followed by experimental results obtained using TIE to recover the 3D topograms of CTF-coated fingermarks. Section 4 re-derives the TIE + TPE with consideration of electrically controllable optical path lengths using LCs. Section 5 compares the phase retrieval results of DH + TIE and DH + TIE + TPE with electrically programmable optical path lengths. Section 6 then concludes the paper.

2. CONVENTIONAL TIE, TPE, AND TIE + TPE

TIE can be derived from the approach proposed by Teague and represents the law of light energy conservation [59,60]. The TIE is applied to phase retrieval. It is a partial differential equation (PDE) derived from the Helmholtz equation or paraxial wave equation for the envelope of the optical field $E_e(x, y; z)$ propagating in free space [24]. Upon substituting the optical field as

$$E_p(x, y, z) = E_e(x, y; z)e^{-jk_o z};$$
$$E_e(x, y; z) = \sqrt{I(x, y; z)}e^{-j\varphi(x,y;z)}, \tag{1}$$

and under the assumption of near-uniform intensity, which typically is true for a phase object near the image plane, the PDE takes the form

$$\nabla_\perp^2 \varphi(x, y; z) + k_0 \frac{1}{I(x, y; z)} \frac{\partial I(x, y; z)}{\partial z} \approx 0. \tag{2}$$

In Eq. (2), $\varphi(x, y; z)$ is the phase; $I(x, y; z)$ is the optical field intensity; k_0 is the wavenumber (or propagation constant) and is related to wavelength; $\nabla_\perp^2 = \vec{\nabla}_\perp \cdot \vec{\nabla}_\perp$, where $\vec{\nabla}_\perp$ is the transverse gradient operator; and z denotes the longitudinal distance around the image (or object) plane, which may be denoted as $z = z_0$. Without loss of generality, we can set $z_0 = 0$. The parameter z in an equation like Eq. (2) will be simply replaced by $z = z_0 = 0$, and the z-derivative of a dependent variable such as the intensity $I(x, y; z)$ around $z = z_0 = 0$ will be denoted by $\frac{\partial I(x,y;0)}{\partial z}$. Equation (2) can be solved using the fast Fourier transform (FFT) to obtain the solution of the phase as [84]

$$\varphi(x, y; 0) = \mathcal{F}^{-1}\left\{\frac{1}{k_x^2 + k_y^2}\mathcal{F}\left\{\frac{k_0}{I(x, y; 0)}\frac{\partial I(x, y; 0)}{\partial z}\right\}\right\}, \tag{3}$$

where $\mathcal{F}$ and $\mathcal{F}^{-1}$ are the forward and inverse Fourier transform operators, and k_x and k_y are spatial frequency variables.

Similarly, the TPE can also be derived from the real part of the Helmholtz equation or paraxial wave equation and incorporates the effect of diffraction [84]. It is expressed as [88]

$$\vec{\nabla}_\perp \varphi(x, y; 0) \cdot \vec{\nabla}_\perp \varphi(x, y; 0) + 2k_0\left(\frac{\partial \varphi(x, y; 0)}{\partial z}\right)$$
$$= \frac{\vec{\nabla}_\perp^2 \sqrt{I(x, y; 0)}}{\sqrt{I(x, y; 0)}}. \tag{4}$$

Ideally, the TIE and TPE can be solved recursively to obtain the true solution to phase [81]. It has been recently shown that the TIE solution can be improved by incorporating a correction factor from the TPE without the need for a recursive solution. The non-recursive TIE + TPE can be expressed as [67]

$$\varphi(x, y; 0) = \mathcal{F}^{-1}\left\{\frac{1}{k_x^2 + k_y^2}\mathcal{F}\left\{\frac{k_0\mu(x, y; 0)}{I(x, y; 0)}\frac{\partial I(x, y; 0)}{\partial z}\right\}\right\}, \tag{5}$$

where $\mu(x, y; 0)$ is a correction factor that, under the condition of near constancy of the intensity, is given as [67]

$$\mu(x, y; 0) = 1 + \frac{1}{k_0 \frac{\partial I(x,y;0)}{\partial z}} \vec{\nabla}_\perp I(x, y; 0) \cdot \vec{\nabla}_\perp \varphi(x, y; 0)$$
$$+ \frac{1}{k_0}\frac{\partial \varphi(x, y; 0)}{\partial z}, \tag{6}$$

with $\frac{\partial \varphi(x,y;0)}{\partial z}$ being calculated from the TPE in Eq. (4). Equation (6) shows the local refractive index $\mu(x, y; 0)$ in the TIE, which can be thought of as the virtual refractive index profile of an effective inhomogeneous medium due to nonuniformity in the intensity profile, can be adapted and utilized as a correction in the TIE. The TIE is solved once again using the correction factor and shows a reduction of errors upon applying Eq. (6).

A. Example: Unwrapped Image Phase Retrieval Using TIE, TIE + TPE

Simulations done by Zhou *et al.* [67,84] have shown conclusively that phase retrieval using the non-recursive TIE + TPE method results in a reduction of errors compared to the TIE alone. The errors that are reduced by the correction factor in the TIE + TPE method are those stemming from the finite difference estimation of the axial intensity derivative at the image plane and the nonuniformity of the intensity at the image plane. Recall that the derivation of Eq. (2) relies on the assumption of uniform intensity at the image plane so that the intensity term $I(x, y; 0)$ can be pulled outside of the transverse gradient operator. Under the constant-intensity assumption, $\vec{\nabla}_\perp I(x, y; 0) = 0$ and $\frac{\vec{\nabla}_\perp^2 \sqrt{I(x,y;0)}}{\sqrt{I(x,y;0)}} = 0$, meaning that the correction factor of Eq. (6) can be rewritten as

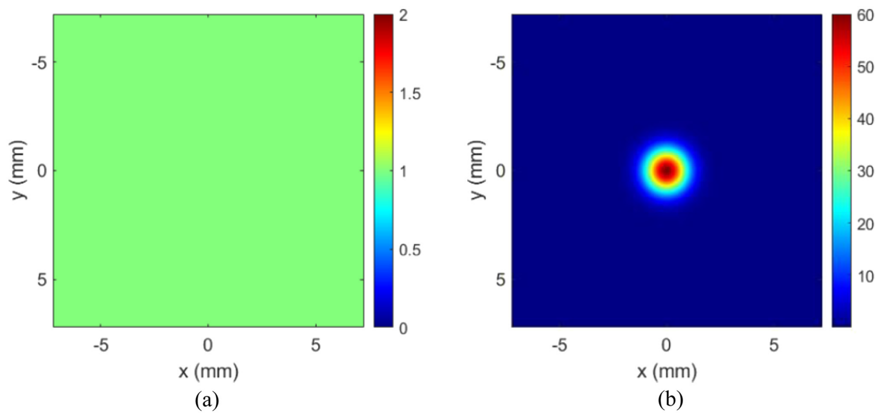

Fig. 1. (a) Intensity and (b) phase of the designed Gaussian phase object for simulation. The intensity is designed as a uniform distribution, which indicates the object is an ideal phase object. The maximum phase value of the Gaussian phase is 60 rad with a width of 1 mm [84].

$$\mu(x, y; 0) = \sqrt{1 + \frac{1}{\sqrt{I(x, y; 0)}} \frac{\partial^2 \sqrt{I(x, y; 0)}}{\partial z^2} - \frac{1}{k_0} \vec{\nabla}_\perp \varphi(x, y; 0) \cdot \vec{\nabla}_\perp \varphi(x, y; 0)}, \tag{7}$$

where the axial derivative of the phase substituted into Eq. (6) is given by

$$\frac{\partial \varphi(x, y; 0)}{\partial z} = \sqrt{k_0^2 + \frac{1}{\sqrt{I(x, y; 0)}} \frac{\partial^2 \sqrt{I(x, y; 0)}}{\partial z^2} - \vec{\nabla}_\perp \varphi(x, y; 0) \cdot \vec{\nabla}_\perp \varphi(x, y; 0)} - k_0. \tag{8}$$

Simulations are done for a pure phase object having a Gaussian phase distribution and uniform amplitude at the image plane $z = 0$. The simulated object is an array of 2880×2880 pixels with 5 μm pitch, illuminated with 650 nm wavelength coherent light, and the Gaussian phase has a peak of 60 rad and a width of 1 mm as shown in Fig. 1.

When the object is located at the plane $z = 0$, the convolution between the object field and the impulse response for propagation gives the optical field at the two defocused planes, from which the intensity is easily found [84]. The defocus distance used in these simulations is $\Delta z = \pm 10$ μm, and the three intensity images at the planes $z = -\Delta z, 0, \Delta z$ are shown in Figs. 2(a)–2(c), respectively. From the three intensity images, the phase distribution at the focal plane is found using the FFT-based TIE and shown in Fig. 2(d).

The recovered phase distribution, along with the three intensity images, is now employed to calculate the correction factor as defined in Eq. (7). Once calculated, the correction factor is substituted into the updated TIE + TPE, Eq. (5), which is solved to recover the phase distribution. The comparison of the phase distributions recovered from the FFT-based TIE and TIE + TPE methods for a uniform amplitude Gaussian phase object is shown in Figs. 3(a) and 3(b), respectively.

To quantitatively determine which method performs better, they are analyzed using the root mean square error (RMSE), defined as

$$\text{RMSE} = \sqrt{\frac{1}{M \times N} \sum_{i'=1}^{M} \sum_{j'=1}^{N} \left[\varphi_{\text{retrieved}}(i', j') - \varphi_{\text{ground truth}}(i', j')\right]^2}, \tag{9}$$

where $M = N = 2880$, the number of pixels in each dimension; $\varphi_{\text{ground truth}}(i', j')$ is the phase of the Gaussian phase object with peak phase of 60 rad and a width of 1 mm; and $\varphi_{\text{retrieved}}(i', j')$ is the recovered phase profile at the focal plane. The RMSE metric is used to compare the two methods to the ground truth, with a smaller value meaning a closer match, or less error. The RMSE value for the FFT-based TIE and TIE + TPE methods, respectively, are 3.87×10^{-3} rad and 1.11×10^{-3} rad, confirming that the TIE + TPE outperforms the FFT-based TIE with a 67% reduction in error for a uniform amplitude Gaussian phase object.

Next, the TIE + TPE phase retrieval is tested against an object with non-uniform intensity, and RMSE between the ground truth phase and the recovered phase is compared to that of the FFT-based TIE. To simulate the non-uniform intensity at the focal plane [see Fig. 4(a)], a Gaussian profile with peak amplitude of 0.01 rad and width of 1 mm is added to the uniform intensity profile seen in Fig. 1(a), with the phase profile remaining the same as in Fig. 1(b). Since the intensity is non-uniform at the focal plane, the relations $\vec{\nabla}_\perp I(x, y; 0) = 0$ and $\frac{\vec{\nabla}_\perp^2 \sqrt{I(x,y;0)}}{\sqrt{I(x,y;0)}} = 0$ are no longer valid, meaning the correction factor and axial phase derivative shown in Eqs. (7) and (8) do not apply. Instead, the correction factor shown in Eq. (6) is used, and the axial phase derivative $\frac{\partial \varphi(x,y;0)}{\partial z}$ can be found by rearranging Eq. (4). After this, the same process is followed to recover the phase of the object for both the FFT-based TIE method and the TIE + TPE method, results of which are shown in Figs. 4(b) and 4(c), respectively. One-dimensional line profiles taken from Figs. 4(b) and 4(c) are plotted and shown in Fig. 4(d) along with the ground truth phase of the simulated object. The insets of

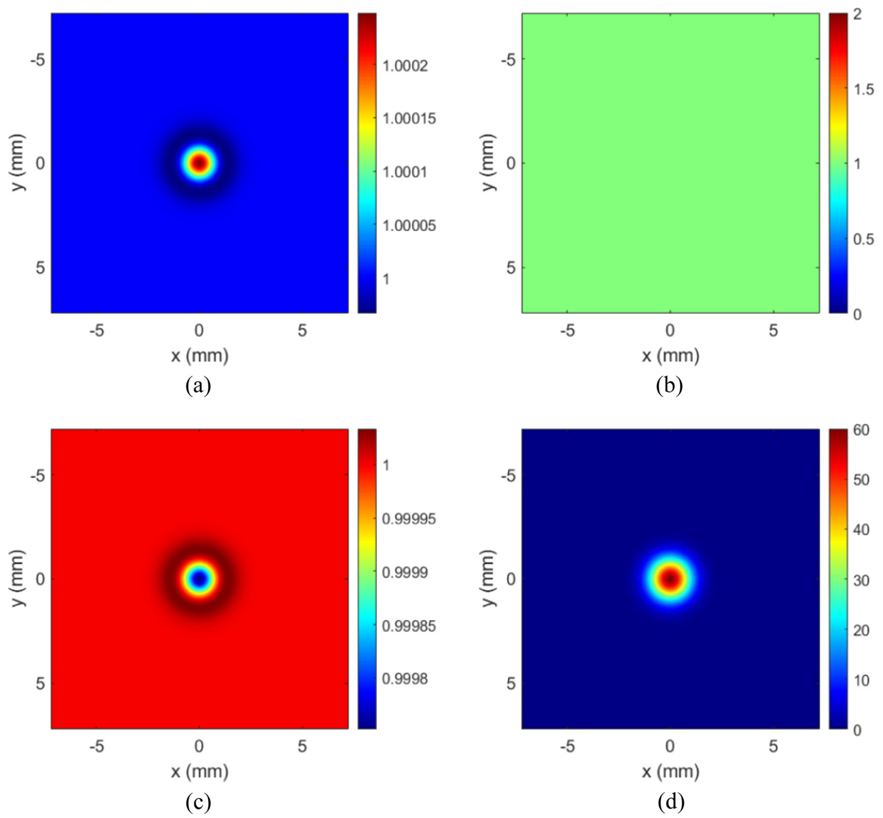

Fig. 2. Generated intensity images at the plane (a) $z = -\Delta z$; (b) $z = 0$; (c) $z = +\Delta z$. (d) Phase distribution at the image plane $z = 0$ computed by FFT-based TIE [84].

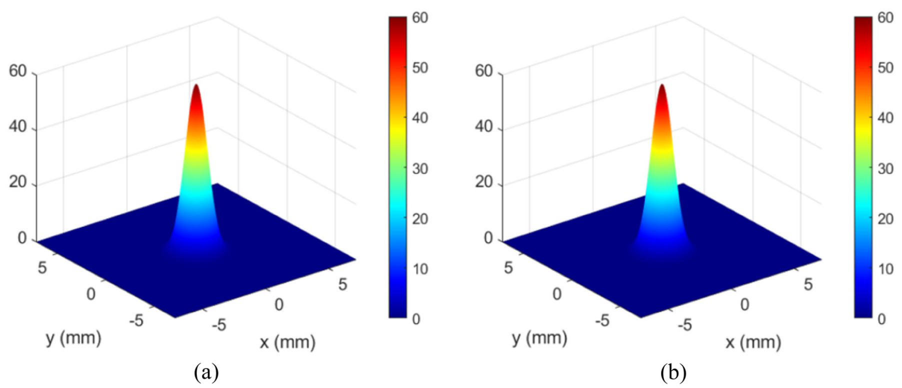

Fig. 3. Phase retrieval results using FFT-based (a) TIE and (b) TIE + TPE for the Gaussian phase object having a maximum phase of 60 rad and a width of 1 mm [84].

Fig. 4(d) show a more detailed comparison between the phase retrieval methods.

The RMSEs are calculated between the retrieved phase and ground truth phase for each method, giving 0.3057 rad for the FFT-based TIE and 0.1842 rad for the TIE + TPE, showing again the superiority of the latter.

3. UNWRAPPED PHASE RETRIEVAL DURING IMAGE RECONSTRUCTION FROM OFF-AXIS DIGITAL HOLOGRAM USING TIE

As discussed in Section 2, the TIE solution for the phase around the image plane can be written as [109]

$$\begin{aligned}
&\varphi(x, y; 0) \\
&= \mathcal{F}^{-1}\left\{\frac{1}{k_x^2 + k_y^2}\mathcal{F}\left\{\frac{k_0}{I(x, y; 0)}\frac{\partial I(x, y; 0)}{\partial z}\right\}\right\} \\
&\approx \mathcal{F}^{-1}\left\{\frac{1}{k_x^2 + k_y^2}\mathcal{F}\left\{\frac{k_0}{\Delta z}\frac{I(x, y; \Delta z) - I(x, y; -\Delta z)}{I(x, y; \Delta z) + I(x, y; -\Delta z)}\right\}\right\}.
\end{aligned} \quad \textbf{(10)}$$

From a preliminary verification, we observe that using $I(x, y; 0) = [I(x, y; \Delta z) + I(x, y; -\Delta z)]/2$ has a better accuracy performance than using $I_0(x, y; 0)$, which is the captured image plane intensity. The various intensities on the

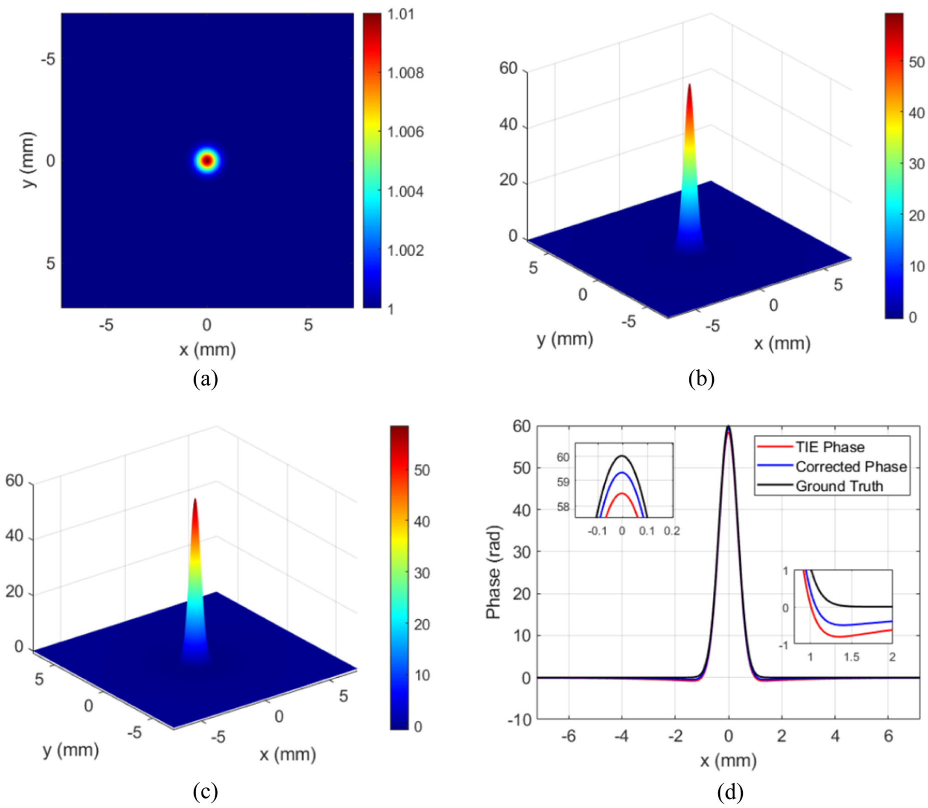

Fig. 4. (a) Non-uniform intensity profile of simulated object used to test the performance of the TIE + TPE phase retrieval method. Phase retrieval results using (b) TIE + TPE and (c) FFT-based TIE for object with phase in Fig. 1(b) and intensity in (a). (d) Extracted line profiles across the center of (b) and (c) along the x-axis. The insets are the zoomed-in plots of the Gaussian phase peak and the right edge of the lobe [84].

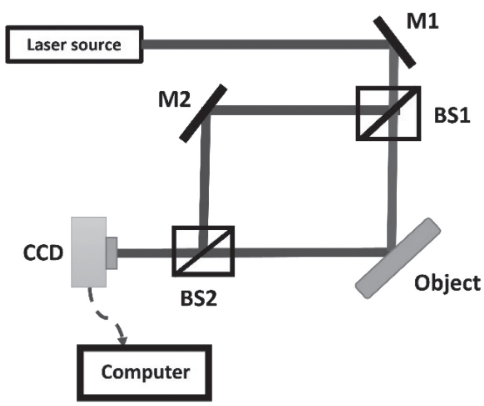

Fig. 5. Schematic of experimental setup used to record digital holograms, where M1 and M2 are planar mirrors, and BS1 and BS2 are 50/50 beam splitters.

right side of Eq. (10) needed to calculate $\frac{\partial I(x,y;0)}{\partial z}$ around the reconstruction plane can be obtained during reconstruction from a digital hologram simply by numerical propagation through defocusing distances $\pm\Delta z$ around the image plane. Equation (10) shows no phase unwrapping is needed during phase retrieval using TIE [109]. The concept of DH + TIE consists of three steps [109]:

1. recording the digital hologram from the object as shown in Fig. 5;
2. reconstructing intensity profiles at two slightly defocused planes around the image plane; and
3. employing TIE using these intensity images to retrieve the unwrapped phase and, hence, the object's topography.

All the simulations for numerical propagation of the optical fields, including reconstruction of digital holograms, are done using MATLAB software. Simulations are done by applying the FFT algorithm [84].

A. Example 1: Simulation of Unwrapped Phase Retrieval from Off-Axis Digital Hologram Using TIE

Simulating the unwrapped phase retrieval from an off-axis digital hologram using TIE requires first that we simulate the hologram, which is referred to as a computer-generated hologram (CGH) [107]. The object has uniform intensity, and a Gaussian phase profile with a width of 0.5 mm and peak phase of 60 radians simulated using a 1024×1024 array with 4.65 μm pixel pitch, as shown in Fig. 6. The object field at the object plane $z = 0$ is written as $E_{o0}(x, y) = E_o(x, y; z = 0) = A_0(x, y)e^{-j\varphi_0(x,y)}$, with $|A_0(x, y)|^2$ representing the uniform intensity in Fig. 6(a), and $\varphi_0(x, y)$ representing the Gaussian phase profile shown in Fig. 6(b). The plane wave reference field at the hologram plane $z = d$ is written as $E_r(x, y; z = d) = A_r(x, y)e^{-j\varphi_r(x,y)}e^{-j(k_{0x}x+k_{0y}y)}$, where $A_r(x, y), \varphi_r(x, y)$ represent the amplitude and phase of the reference field, respectively, and are taken to be constants in these

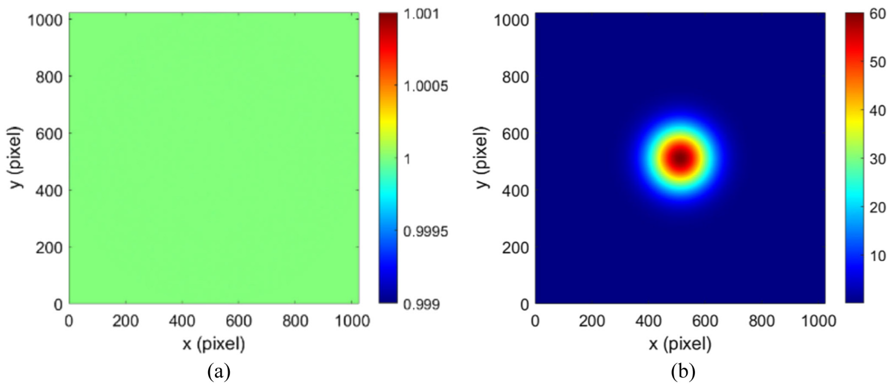

Fig. 6. Simulated object with uniform intensity and a Gaussian phase profile having a maximum phase value of 60 rad and width of 0.5 mm, for a wavelength of 514.5 nm. (a) Intensity of the object; (b) phase of the object [107].

simulations. The terms $k_{0x} = k_0 \sin(\theta_x)$ and $k_{0y} = k_0 \sin(\theta_y)$ are the carrier frequencies introduced by the slight angular deviation of the reference field with respect to the propagation vector of the object field in the off-axis DH configuration, where θ_x and θ_y are the tilt angles in the x and y directions, respectively, and $k_0 = 2\pi/\lambda$ is the wavenumber for a wavelength of $\lambda = 514.5$ nm [107].

The recorded hologram is the interference of the diffracted object field $E_{od}(x, y; z = d)$ and the plane-wave reference field $E_r(x, y; z = d)$ at the hologram plane $z = d$. The diffracted object field is calculated by a convolution of the original object field with the impulse response of propagation, giving

$$E_{od}(x, y) = E_o(x, y; z = d) = E_{o0}(x, y) * h_p(x, y; z = d), \tag{11}$$

where the asterisk ($*$) denotes the convolution operation and the impulse response for propagation $h_p(x, y; z)$ is given by [105]

$$h_p(x, y; z) \propto \frac{e^{-jk_0\sqrt{x^2+y^2+z^2}}}{\sqrt{x^2+y^2+z^2}}. \tag{12}$$

The hologram function can be approximated to within a proportionality constant by the intensity of the interference between the diffracted object field and the tilted plane-wave reference field, resulting in the simulated or computer-generated hologram (CGH) function [see Fig. 7(a)]

$$\begin{aligned} h_{\varphi_r}(x, y; d) &\propto \left| E_{od}(x, y) + A_r(x, y) e^{-j\varphi_r(x,y)} e^{-j(k_{0x}x+k_{0y}y)} \right|^2 \\ &= |E_{od}(x, y)|^2 + A_r^2(x, y) + E_{od}(x, y) A_r(x, y) \\ &\quad \times e^{j\varphi_r(x,y)} e^{j(k_{0x}x+k_{0y}y)} \\ &\quad + E_{od}^*(x, y) A_r(x, y) e^{-j\varphi_r(x,y)} e^{-j(k_{0x}x+k_{0y}y)}. \end{aligned} \tag{13}$$

The first two terms in Eq. (13) correspond to the zeroth-order, or dc, components of the diffracted object and plane-wave reference fields, respectively, while the third term contains the object information we desire, and the fourth term is a twin image of the third term. Concentrating on the third term (virtual image), it must be isolated from the dc terms and twin image term. This can easily be done in the spatial frequency domain by applying a bandpass filter [107], after which the chosen spectrum is centered, zero-padded back to the original array size, and then multiplied by the plane-wave reference field to obtain the reconstructed object field at the hologram plane $z = d$. Then, back-propagation is used to get the reconstructed object field at and around the object plane, namely, at $z = -\Delta z$, 0, and Δz, with Δz chosen to be 0.1 mm for these simulations. From the object field reconstructions at the planes $z = -\Delta z$, 0, and Δz, one easily obtains the three respective intensity images $I_{-1}(x, y)$, $I_0(x, y)$, and $I_1(x, y)$.

From here, the two reconstructed intensity images at the defocus planes $\pm\Delta z$, respectively shown in Figs. 7(b) and 7(c), are used with the TIE, under the assumption of uniform intensity at the object plane, to recover the unwrapped phase of the object. Using Eq. (11), the unwrapped phase of the object under the conditions (a) $I(x, y) = I_0(x, y)$ and (b) $I(x, y) = \frac{I_1(x,y)+I_{-1}(x,y)}{2}$ are found and compared with the phase recovered from using single-wavelength DH (SWDH) after employing the PUMA phase unwrapping algorithm. The recovered phases for the three methods are shown in Fig. 8. The mean square error (MSE) between the recovered phase and the ground truth phase of the simulated object is used as a performance metric to compare each of the methods. The results are listed in Table 1.

B. Example 2: Phase Retrieval and Fingermark Topography Using Off-Axis DH and TIE

This subsection presents a combination of DH and TIE methods to acquire and analyze fingermark specifics [109]. A typical off-axis setup for holographic recording where the object field is light reflected from a CTF-coated fingermark is utilized to digitally record holograms of partial bloody fingermarks [109,110]. Different fingermarks, such as environmentally stressed [111,112] and partially bloody fingermarks [113] on a diversity of nonporous substrates, are first developed by coating with nanoscale CTFs. The choice of CTFs has been shown to preserve height unlike a simple thin film. Also, CTFs of simple metals and dielectrics have been tried, and the materials best suited for a given substrate have been used, viz., chalcogenide glass for the substrates under investigation [114,115].

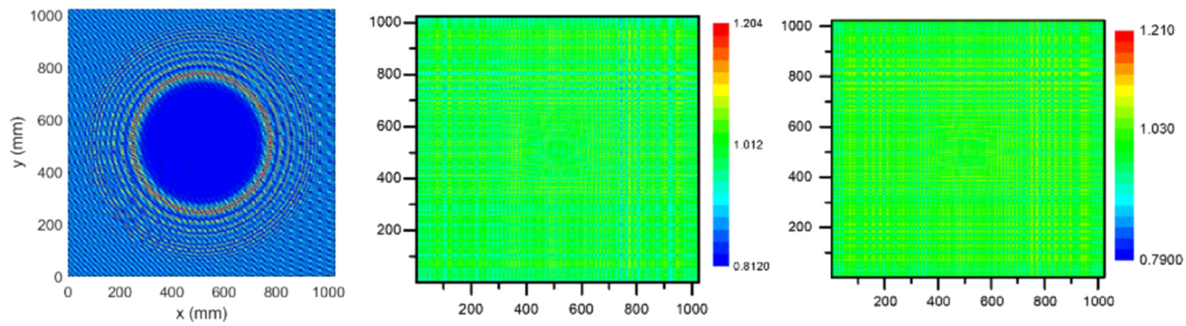

(a) (b) (c)

Fig. 7. (a) CGH generated from an off-axis setup; simulated digital hologram of the simulated object with uniform intensity and Gaussian phase profile having a peak phase of 30 rad and width of 0.5 mm. Reconstructed intensity images at the plane of (b) $z = \Delta z$ and (c) $z = -\Delta z$ [107].

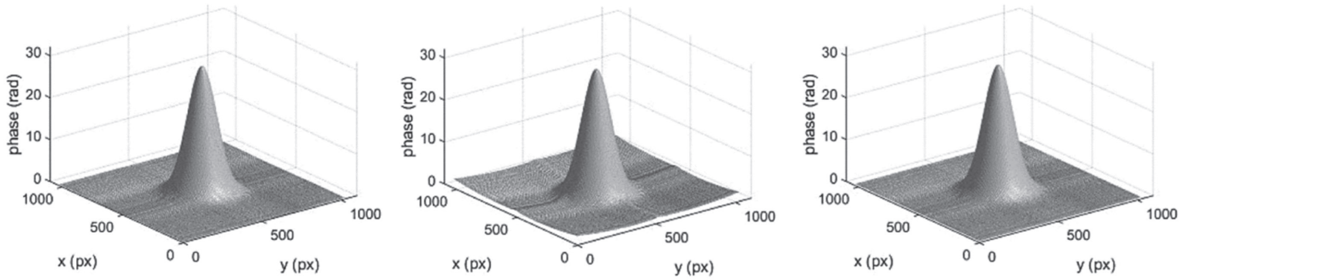

(a) (b) (c)

Fig. 8. Retrieved phase using off-axis DH + TIE: (a) $I(x, y) = I_0(x, y)$ and (b) $I(x, y) = \frac{I_1(x,y)+I_{-1}(x,y)}{2}$ for an object with Gaussian phase profile and peak phase of 30 rad. (c) Retrieved phase using SWDH after unwrapping with PUMA for the same object in (a) and (b) [107].

Table 1. MSE for Off-Axis DH and DH + TIE Reconstructions

Method	MSE (5 rad)	MSE (30 rad)	MSE (60 rad)
DH + TIE ($I = I_0$)	0.0098	0.0070	0.0039
DH + TIE ($I = \frac{I_{+1}+I_{-1}}{2}$)	0.0697	0.0843	0.1118
SWDH	0.0069	0.0070	0.0070

A hologram is recorded with the coherent laser light from an Ar-ion laser tuned to $\lambda = 514.5$ nm. For recording the hologram, a modified Mach–Zehnder interferometer previously shown schematically in Fig. 5 is used. A detailed setup is illustrated in Fig. 9(a). The laser beam is collimated and expanded by a spatial filter assembly and a collimation lens with a 250 mm focal length. The CCD camera (Thorlabs, DCU223C) has a resolution of 1024 × 768 pixels with a pixel pitch of 4.65 μm along both x and y axes. A slight angle is introduced between the

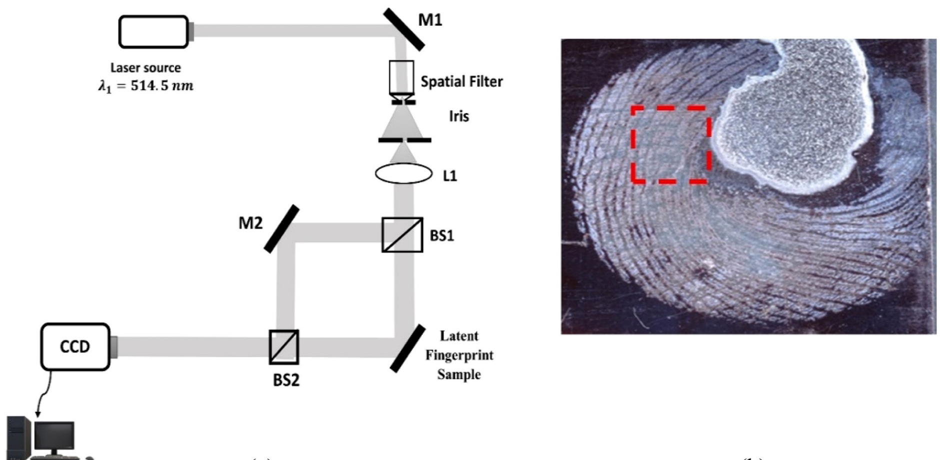

(a) (b)

Fig. 9. (a) Schematic of experimental setup used to record digital holograms of CTF-coated fingermarks, where M1 and M2 are planar mirrors, and BS1 and BS2 are 50/50 beam splitters. The distance between the fingermark sample and the CCD camera is $d = 40$ cm. (b) The object is a partial bloody fingermark on a glass slide on which an ∼1000-nm- thick CTF of chalcogenide glass [113] has been deposited. The red box shows the illuminated region for hologram recording.

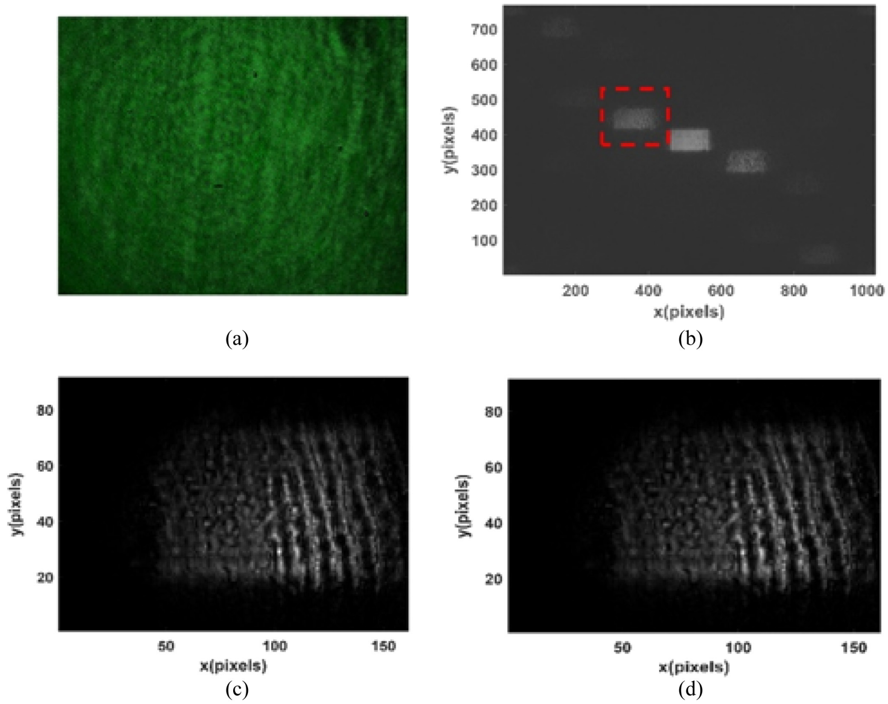

Fig. 10. (a) Typical recorded off-axis hologram with wavelength $\lambda = 514.5$ nm; the hologram was recorded at a recording distance $d = 40$ cm. (b) Intensity profiles after back-propagation by applying the Fresnel diffraction formula from the hologram plane to the reconstruction plane to find the reconstructed object at the image plane, with the red box indicating the cropped virtual image; (c) reconstructed intensity profile around image plane at $+\Delta z$; (d) reconstructed intensity profile around image plane at $-\Delta z$. These defocused intensity profiles are obtained numerically at the focused and defocused planes as $\Delta z = \pm 0.001$ mm.

reference and object beams, in this case about 1.5°, to separate the reconstructed image from the zeroth order. The distance from the sample to the CCD camera is 40 cm.

The object comprises a partially bloody fingermark on a glass slide and is encapsulated by an ~1000-nm-thick CTF of chalcogenide glass, shown in Fig. 9(b) [113]. Only the level-1 and level-2 details in CTF-developed fingermarks can be seen with the naked eye.

The acquired hologram from the experiment is shown in Fig. 10(a), which is reconstructed by applying the Fresnel propagation technique. Due to the off-axis setup for hologram recording, back-propagation to the original object plane will generate three distinct patches of light: the DC or central patch, the in-focus virtual image, and the out-of-focus real image. A typical reconstruction using back-propagation is shown in Fig. 10(b). Then, one of the sidebands after reconstruction is cropped, as demonstrated by a red box in Fig. 10(b). Now knowing the optical field at the image plane, the optical profiles, and hence intensity profiles, due to propagational diffraction, are numerically computed at $\pm\Delta z$, where $\Delta z = 0.001$ mm, as shown in Figs. 10(c) and 10(d). These intensity images are employed in TIE to retrieve the phase map for the partial bloody fingermark using Eq. (11) [109].

When the unwrapped phase was computed using TIE, an overall quadratic phase was noted, possibly coming from unwanted phase curvatures introduced by lenses used in the hologram recording setup or diffraction of the reference beam. The quadratic phase should be removed to obtain accurate phase information, including the correct depth value. Removing the quadratic phase can be done by the MATLAB tool "detrend( )." After applying the detrend tool, the final phase result becomes much smoother. Then, the phase $\varphi(x, y)$ is converted to the depth profile $h(x, y)$ using $h(x, y) = \frac{\lambda\varphi(x,y)}{2\pi} \cos\theta$, where $\theta \approx 45°$ is the illumination angle of the object [91,109]. The 2D topography depth profile from the hologram at $\lambda = 514.5$ nm of a CTF-developed fingermark is shown in Fig. 11(a), corresponding to the region on the fingermark sample indicated in Fig. 11(b). Level-3 details, such as pores and ridge bifurcations, can be observed distinctly; more on this will be described later. The calculated typical local depth of pores is approximately ≈ 1.5 µm. Note that 3D information is still partially recoverable near the central dark patch, a blotch of blood in the fingermark that is visible to the naked eye when held up to the light. Figure 11(c) is a 3D rendering of Fig. 11(a). Finally, a typical line-scan across the topography is shown in Fig. 11(d).

We have repeated DH + TIE on the same fingermark sample using a setup similar to Fig. 9(a), but now with a different wavelength $\lambda = 476.5$ nm. By applying DH + TIE, level-3 details for CTF-developed latent fingermarks can be seen clearly, both at $\lambda = 514.5$ nm and $\lambda = 476.5$ nm. Both retrieved topograms of the depth profile are shown side by side in Figs. 12(a) and 12(b); the red circles identify the pores. The depth of the pores is computed to be around 1.8 µm. The red rectangles indicate ridge bifurcations. Initial results of DH with TIE + TPE yield similar topography, with typical depth of pores now being around 2.1 µm. In future work, DH with TIE + TPE results will be compared point by point with those from DH + TIE,

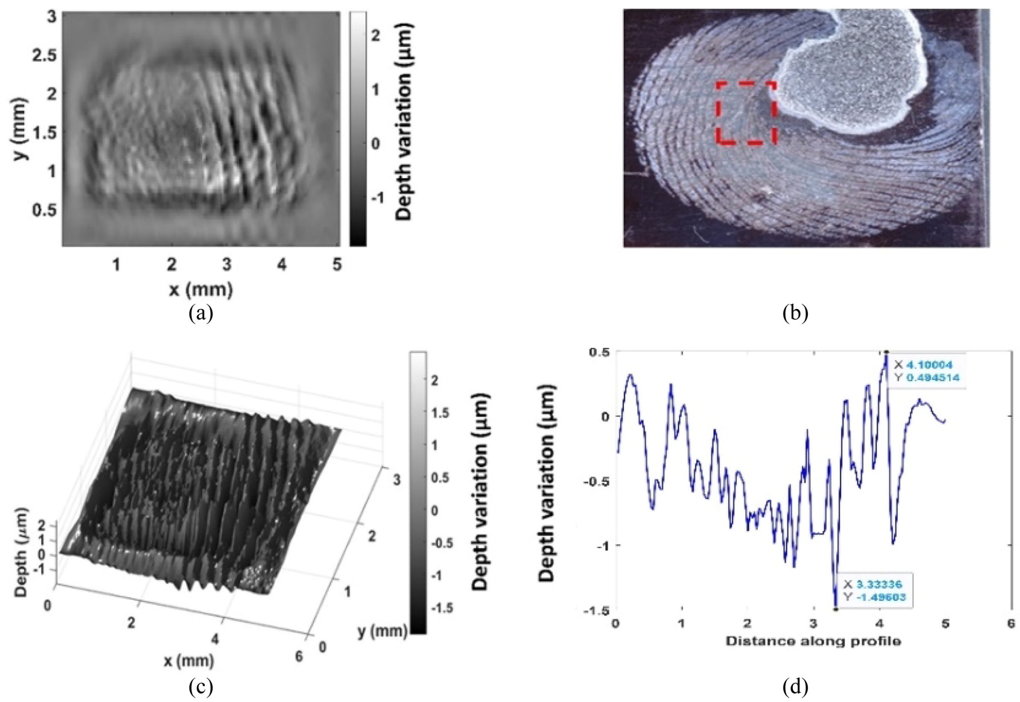

Fig. 11. (a) Topography of depth profile from hologram of fingermark recorded at $\lambda = 514.5$ nm using DH + TIE; (b) microscope image of CTF-developed fingermark samples; the red box shows approximate illuminated region for digital hologram recording. (c) 3D rendering of topography depth profile in (a); (d) typical line-scan across the reconstructed 3D topogram [116].

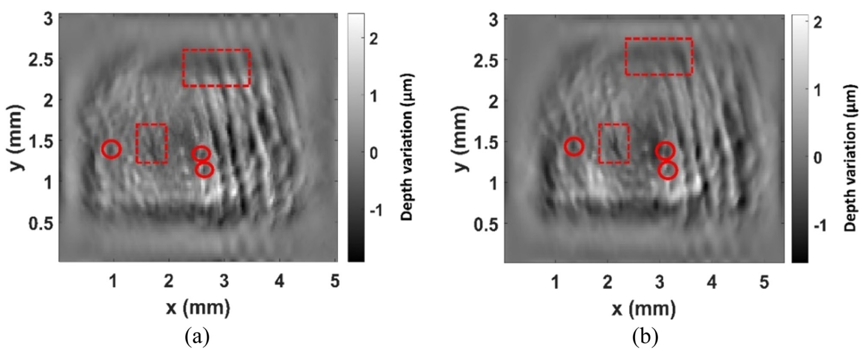

Fig. 12. 2D topography of depth profile using DH + TIE at (a) $\lambda = 514.5$ nm and (b) $\lambda = 476.5$ nm. The red circles identify the pores, while the red rectangles indicate ridge bifurcations [116].

and DH with TIE + TPE will be used to enhance the accuracy of the level-3 details [116].

4. TIE AND TPE WITH ELECTRICALLY PROGRAMMABLE OPTICAL PATH LENGTHS

As seen above, the conventional TIE and TPE show the variation of intensity and phase with propagation distance z [67,84]. As mentioned before, a disadvantage of the TIE is that the intensities need to be registered around the recording plane (often, the image plane) by physically moving the CCD camera, which can lead to alignment issues when superposing the intensities for calculating the longitudinal derivative of the intensity $\frac{\partial I(x,y;z)}{\partial z}$. Instead of monitoring the intensities with propagation distance, the optical path length can be changed by varying the refractive index n of the medium [85–88,108,117]. The TIE, TPE, and hence, the TIE + TPE with electrically programmable optical path lengths can help alleviate the problem of physical movement of the CCD camera by introducing varying path lengths using an EO material, viz., an LC in our case [85–88,117]. The LC facilitates this through a change of refractive index with applied voltage. Linearly polarized light with polarization parallel to the long axis of the LC in a nematic LC device sees different refractive indices as the molecules rotate to reorient with the direction of the electric field, which is applied across the LC in the nominal direction of propagation (z) of the optical field. The change in refractive index results from the birefringence of the LC under applied electrical bias [85–88,108,117]. This is described more in Section 5. In this case, a modified TIE should be derived to describe the intensity-phase relation with the variation of refractive index n due to the birefringence in the LC [85–88,108,117].

The TIE and TPE with electrically programmable optical path lengths can also be considered as a two-stage phase retrieval process [108,117]. As in the conventional case discussed above, in the first stage, the FFT method is applied to retrieve the phase by recording the intensities for different applied voltages across the LC sample. In the second stage, a correction factor is introduced as in the case of the non-recursive TIE + TPE described earlier. The TPE method is utilized to determine the longitudinal phase derivative in the correction factor. Then, the TIE is modified with the correction factor to obtain the phase retrieval [108,117].

The modified TIE and TPE can be derived by starting from the paraxial wave equation considering a coherent monochromatic optical field propagating along the z-axis, passing through (or reflected from) an object and then immediately passing through an LC with thickness d, refractive index $n(V)$, and birefringence $\Delta n(V)$, thereby providing the equivalent of translation through a distance z. The voltage V across the LC gives rise to birefringence, and hence a voltage-dependent refractive index through the rotation of the director axis. Details of the derivation are provided in Alanazi and Banerjee [117]. Following Gupta *et al*. [85,86], the TIE with LC can be derived from the traditional TIE but suitably modified to include the variation in the refractive index, and hence the optical path length, instead of the physical path length. The modified TIE with LC then gives the phase expressed as

$$\varphi(x, y; n) = \mathcal{F}^{-1}\left\{\frac{1}{k_x^2+k_y^2}\mathcal{F}\left\{\frac{k_o n^2}{d}\frac{1}{I(x, y; n)}\frac{\partial I(x, y; n)}{\partial n}\right\}\right\}. \tag{14}$$

The correction factor can be obtained from the TPE, again suitably modified to include the variation in the refractive index, and hence the optical path length, instead of the physical path length. As detailed by Alanazi and Banerjee [117], the modified TIE + TPE with LC gives

$$\varphi(x, y; n) = \mathcal{F}^{-1}\left\{\frac{1}{k_x^2+k_y^2}\mathcal{F}\left\{\frac{k_o n^2}{d}\mu(x, y; n)\frac{1}{I(x, y; n)} \times \frac{\partial I(x, y; n)}{\partial n}\right\}\right\}, \tag{15}$$

where n denotes the average refractive index and where the correction factor $\mu(x, y; n)$ can be found as [117]

$$\mu(x, y; n) \approx \left(1+\frac{1}{n^2}\right) - \frac{1}{k_o n^2 d}\frac{\partial\varphi(x, y; n)}{\partial n} - \frac{d}{k_o n^2}\frac{1}{\frac{\partial I(x,y;n)}{\partial n}} I(x, y; n)\,\nabla_\perp^2\varphi(x, y; n). \tag{16}$$

In an actual experiment or simulation, two bias voltages can be assumed to be applied across the LC to introduce the change in the refractive index. For computational convenience, Eq. (15) can be rewritten as

$$\varphi(x, y; n) = \frac{2k_0 n^2}{d} \times \mathcal{F}^{-1}\left\{\frac{1}{(k_x^2+k_y^2)}\mathcal{F} \times \left\{\frac{1}{I(x, y; n(V_1)) + I(x, y; n(V_2))}\mu(x, y; n) \times \frac{I(x, y; n(V_2)) - I(x, y; n(V_1))}{\Delta n_2 - \Delta n_1}\right\}\right\}, \tag{17}$$

where $I(x, y; n)$ in Eq. (17) has been replaced with the average value of intensities for two applied voltages, and $\Delta n_2 - \Delta n_1 = n(V_2) - n(V_1)$. The quantity Δn represents the birefringence of the LC. For an appropriately polarized illumination (along the true alignment of the LC molecules), and past the threshold voltage, the refractive index seen by the optical field in the LC will reduce as the voltage across the LC is increased. The decrease will be by an amount equal to the voltage-induced birefringence as the molecules orient themselves more along the direction of the applied voltage across the LC, assumed to be the direction of propagation.

A. Summary of Liquid Crystal Characteristics Used for Simulations and Experiments

A nematic LC fabricated in-house and characterized in the lab is used for experiments [117]. Also, the calculated refractive index change with voltage is used to perform numerical simulations with realistic values of the change in the optical path length (OPL) [117–120]. The fabricated LC cell consists of a thin 5CB LC layer with a thickness of 40 µm sandwiched between a pair of alignment layers with a thickness of 20 nm, which are coated with 200 nm layers of a transparent conductive material such as indium-tin-oxide (ITO), and all these materials are placed in a container with two glass plates [117]. The ordinary and extraordinary refractive indices of the 5CB nematic LC cell are 1.544 and 1.736, respectively. We have experimentally determined the *Frédericksz* transition threshold voltage as $V_{th} \approx 1$ V, which is in good agreement with the theoretically calculated value of by $V_{th} = \pi\sqrt{\frac{K_{11}}{\varepsilon_0 \Delta\varepsilon_{LC}}} \approx 0.8$ V, where $K_{11} \approx 6.2$ pN is the bend elastic constant, which is a parameter characterizing the elastic interaction between the nematic molecules, $\Delta\varepsilon_{LC} \approx 12.04$ at 1 kHz and 25°C is the anisotropy of the relative permittivity for pure 5CB, and $\varepsilon_0 = 8.854 \times 10^{-12}$ F/m [121–125].

The birefringence Δn as a function of the voltage V applied across the LC cell that is experienced by the incident optical beam is given by [114,115]

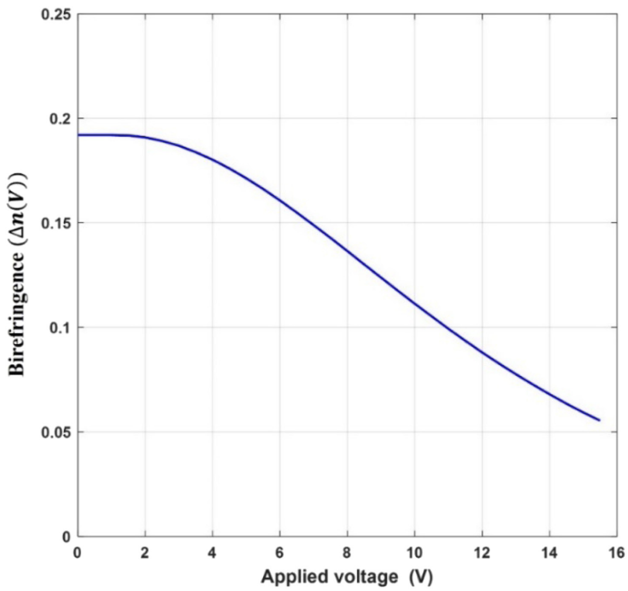

Fig. 13. Variation of birefringence as a function of voltage across the LC [117].

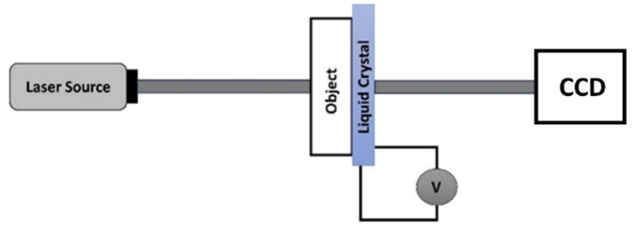

Fig. 14. Schematic diagram for implementation of TIE with LC and TIE + TPE with LC. The two-lens imaging system between the object and the CCD has been left out for simplicity [117].

the method applies to the case where the object is imaged by, say, a confocal two-lens imaging system where the CCD is now at the image plane, which is the back focal plane of the second lens [126,127].

Traditionally, phase retrieval algorithms such as PUMA can fail to give accurate results when phase (and depth) gradients are large [106]. To investigate the performance of TIE + LC and TIE + TPE with LC for the reconstruction of phases (and topographies) with sharper edges, we consider a super-Gaussian, which has larger spectral content and tends to a top hat function for higher values of the order m. The super-Gaussian phase considered here is defined as [128]

$$\Delta n(V)=\left[\frac{n_o n_e}{\sqrt{n_o^2\cos^2\left(\frac{\pi}{2}-2\arctan\left[\exp\left(-\frac{V-V_{\mathrm{th}}}{V_o}\right)\right]\right)+n_e^2\sin^2\left(\frac{\pi}{2}-2\arctan\left[\exp\left(-\frac{V-V_{\mathrm{th}}}{V_o}\right)\right]\right)}}\right]-n_o, \tag{18}$$

where, n_o and n_e are the ordinary and extraordinary refractive indices, respectively, and $V_o=2\pi\sqrt{\frac{\pi K_{11}}{\Delta\varepsilon_{\mathrm{LC}}}}$. The estimate of birefringence with respect to the applied voltage across the LC cell is plotted in Fig. 13. The birefringence for 5CB in the visible region varies from 0.05 to 0.20.

5. EXAMPLES OF PHASE RETRIEVAL USING TIE, TIE + TPE WITH LC

A. Numerical Example 1: Imaged Phase Retrieval Using TIE, TIE + TPE with LC

In this subsection, we provide numerical simulation results of phase retrieval using the proposed TIE + TPE with LC as illustrated in Fig. 14. As mentioned previously, the change of birefringence of a 5CB nematic LC is employed for our numerical simulations [117,124,125]. The birefringence plot as a function of the applied voltage across the LC cell with thickness $d=40$ µm as shown in Fig. 13 is used. Specifically, $\Delta n(V_1=3.5\,\mathrm{V})=0.1838$ and $\Delta n(V_2=10\,\mathrm{V})=0.1113$ are used. The LC cell is assumed to be placed against the phase object. A uniform super-Gaussian phase is used as a phase object to investigate the performance of TIE + TPE with electrically programmable optical path lengths and compared with the traditional TIE + TPE [117]. The true width (waist) of the Gaussian is taken to be 0.2 mm and a wavelength of 514.5 nm is assumed. The peak of the true Gaussian phase is taken as 10 radians. The object is designed with a 1024 × 1024 pixel array (to simulate a standard CCD/CMOS array) with a pixel pitch of 5 µm. Although in this case, the measurement plane (CCD) is assumed to be immediately next to the LC and hence the object,

$$\varphi(x,y;0)=\varphi_{\max}\exp\left[-\left(\frac{x^2+y^2}{w_0^2}\right)^m\right];\quad m=2. \tag{19}$$

The super-Gaussian phase is also a good model for large gradients in the height or topography of the object, which may occur in many practical cases of interest. We now present numerical simulation results of phase retrieval using proposed TIE with LC and TIE + TPE with LC and using the same birefringence parameters as that for the example of the Gaussian above. The numerically generated (defocused) intensity images at V_1 and V_2, as shown in Figs. 15(a) and 15(b), are utilized to determine the phase employing TIE with LC using Eq. (14) with $\mu(x,y;n)=1$ and TIE + TPE with LC using Eqs. (16) and (17).

Cross-sectional plots are shown in Fig. 16(a). The original super-Gaussian phase is also superposed, for comparison. Zoomed-in versions of the figure at the peak and the wings are shown in Fig. 16(b) and Fig. 16(c), respectively. Furthermore, the difference between the retrieved phases using TIE + TPE with LC and TIE with LC is also plotted in Fig. 16(d). The difference is less than 1%; however, TIE + TPE with LC yields results closer to the ground truth.

To further quantify the performance of phase retrieval, the normalized root mean square error (NRMSE), defined as [129]

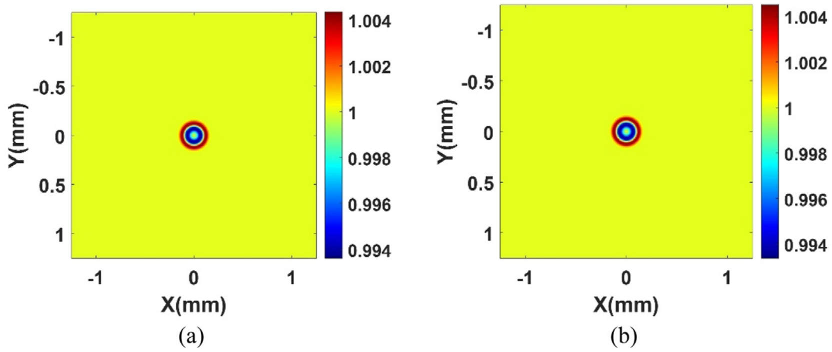

Fig. 15. Numerically generated (defocused) intensity images at V_1 and V_2. The extremum values of intensities are $I(x, y; \Delta n(V_1 = 3.5\text{ V})) = 0.99291\text{ W/m}^2$ and $I(x, y; \Delta n(V_2 = 10\text{ V})) = 0.99185\text{ W/m}^2$ [117].

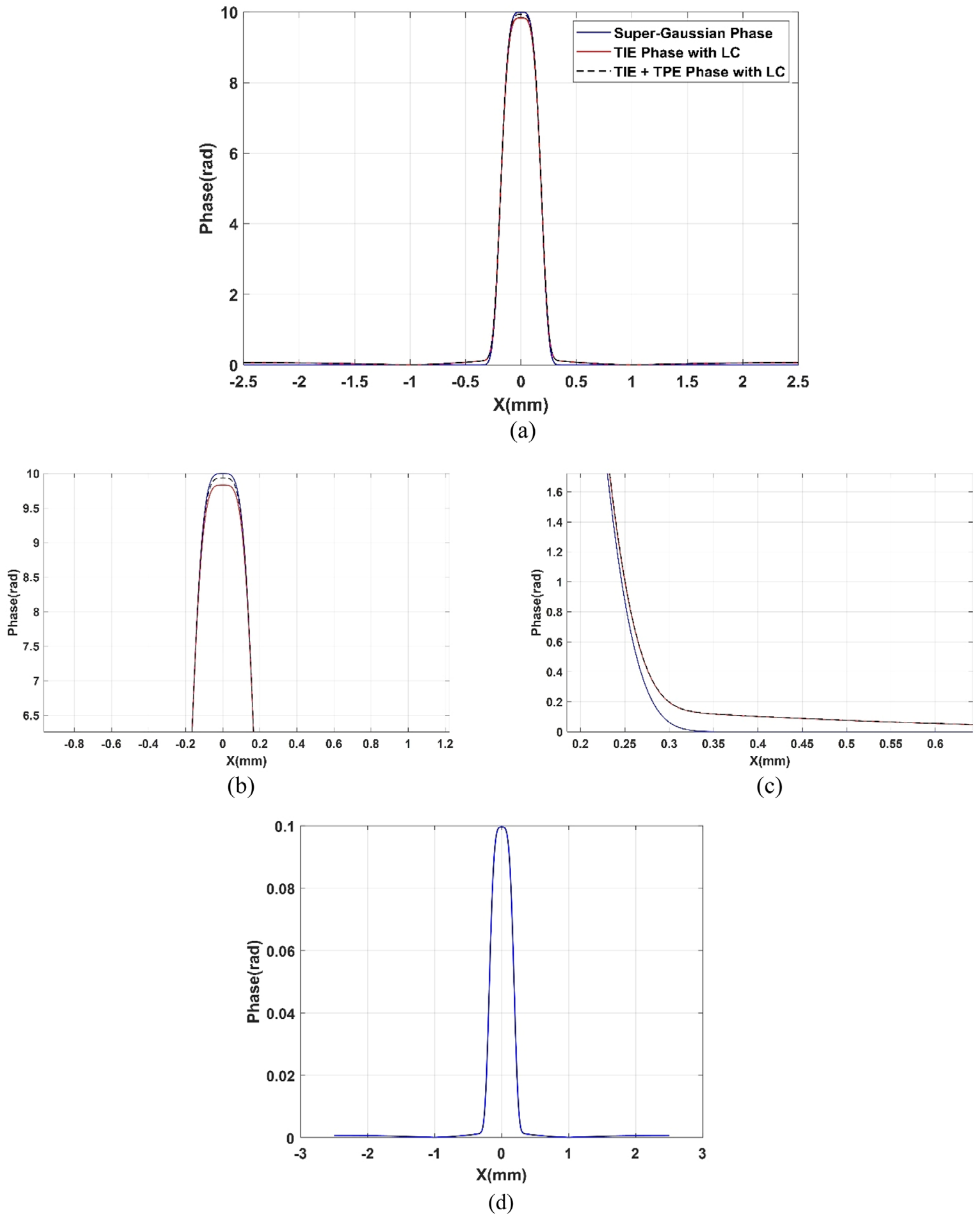

Fig. 16. (a) 1D cross-sectional profiles of the phase from TIE with LC (red) with obtained $\varphi_{\text{max retrieved}} = 9.83$ rad, along with TIE + TPE with LC (black) with obtained $\varphi_{\text{max retrieved}} = 9.93$ rad, along with that of the original super-Gaussian phase (blue). (b) Zoomed-in plots near the Gaussian phase peaks; (c) zoomed-in plots of the wings around the main lobe. (d) Difference phase between TIE + TPE with LC and TIE with LC phase recovery results [117].

Table 2. NRMSEs for Super-Gaussian Phase ($m = 2$) Retrieval

Method	NRMSE
TIE with LC	0.0270
TIE + TPE with LC	0.0242

NRMSE

$$= \frac{\sqrt{\sum_{i'=1}^{M}\sum_{j'=1}^{N}\left[\varphi_{\text{retrieved}}(i', j') - \varphi_{\text{true phase}}(i', j')\right]^2}}{\sqrt{\sum_{i'=1}^{M}\sum_{j'=1}^{N}\left[\varphi_{\text{true phase}}(i', j')\right]^2}}, \quad (20)$$

where M and N are the pixel numbers in the x and y directions, respectively, is computed. Smaller values of NRMSE denote a better reconstruction quality. The NRMSE is computed for each method for super-Gaussian phase retrieval and is shown in Table 2 for $m = 2$. The TIE + TPE with LC performs more accurately than the modified TIE with LC.

B. Numerical Example 2: Phase Retrieval from Off-Axis Digital Hologram and TIE, TIE + TPE with LC

In this example, and to prove the point that TIE and TIE + TPE with LC can be used for holographic imaging as well, unwrapped phase retrieval of the retrieved phase is demonstrated by employing a non-recursive technique involving TIE with LC and TIE + TPE with LC. Here we retrieve a numerically generated super-Gaussian phase recorded with off-axis DH. Our initial results suggest that TIE and non-recursive TIE + TPE with LC provide a more accurate estimate of the imaged phase and hence surface topography during digital hologram reconstruction. The steps in these methods, which mimic the steps in an actual experiment, consist of the following [108]:

1. recording the off-axis digital hologram of the object (assumed here to be a transmissive phase object/screen) against which an LC is considered inserted,
2. reconstructing intensity images around the image plane and for two different values of the applied voltage across the LC cell,
3. retrieving the unwrapped phase by applying TIE with LC, using the reconstructed intensity images,
4. using TIE + TPE with LC to obtain a better estimate of the unwrapped phase.

A super-Gaussian phase of the type [128]

$$\varphi(x, y; 0) = \varphi_{\max} \exp\left\{-\left(\frac{x^2 + y^2}{w_0^2}\right)^m\right\} \quad (21)$$

is considered with $m = 5$ as illustrated in Figs. 17(a) and 17(b), where the parameter m is the order of the super-Gaussian, with $m = 1$ representing the usual Gaussian [70]. The true width (waist) of the super-Gaussian is taken to be 0.2 mm and a wavelength of 514.5 nm is assumed.

Higher values of m correspond to sharper changes in the phase profile, which sometimes cause issues with phase unwrapping by PUMA. In this simulation, the two recorded holograms of super-Gaussian phases are simulated with $V_1 = 3.5$ V and $V_2 = 10$ V corresponding to $\Delta n(V_1) = 0.1838$ and $\Delta n(V_2) = 0.1113$, corresponding to optical path differences $\text{OPL}(V_1) = 0.00735$ mm and $\text{OPL}(V_2) = 0.00445$ mm. In this simulation, the object beam propagates a distance of approximately 25 mm. A small angle of approximately 1.5° is assumed between the reference $R(x, y) \propto \exp[-j(k_{0x}x + k_{0y}y)]$ and object $\exp[-j\varphi(x, y)]$. The optical fields immediately after the object and the LC are given by $\exp[-j\varphi(x, y)] \exp[-jk_0 n(V_{1,2})d]$, and these propagated fields at the recording plane, call them $O'_{1,2}(x, y)$, are used to synthesize two holograms $H_{1,2}(x, y) = |O'_{1,2}(x, y) + R(x, y)|^2$. Next, these holograms are reconstructed through back-propagation to the appropriate image plane, as shown in Figs. 18(a) and 18(b). As is standard during off-axis reconstruction, the twin images are separated by cropping and centering the image of interest (here, virtual). The intensities $I(x, y; n(V_1))$ and $I(x, y; n(V_2))$ at the image plane are reconstructed numerically; these are shown in Figs. 18(c) and 18(d). Then, the TIE with LC and the TIE + TPE with LC are used to compute the phase profile, shown in Figs. 19(a) and 19(b).

Figure 20(a) illustrates the cross-sectional profiles of the original phase of the super-Gaussian phase at different values of the powers $m = 5$ (-red) and modified TIE with LC (-blue), along with DH + TIE + TPE with LC (–green). Figure 20(b) shows zoomed-in plots near the super-Gaussian phase peaks, while

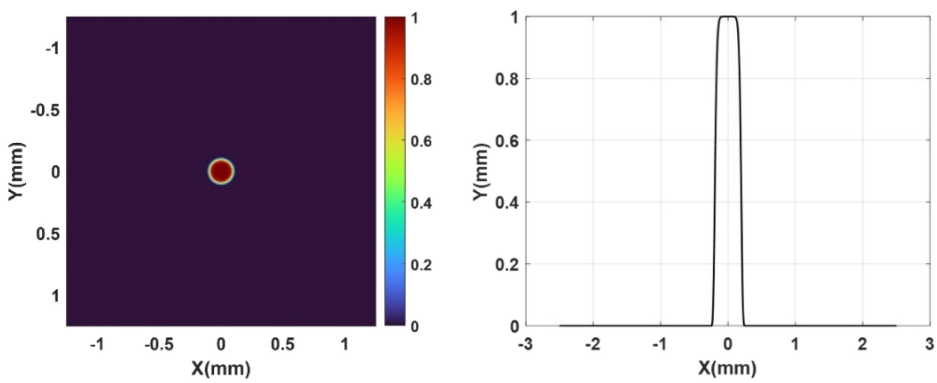

(a) (b)

Fig. 17. (a) True super-Gaussian phase distribution profile; (b) 1D cross-sectional profiles of true phase of the super-Gaussian phase with power $m = 5$.

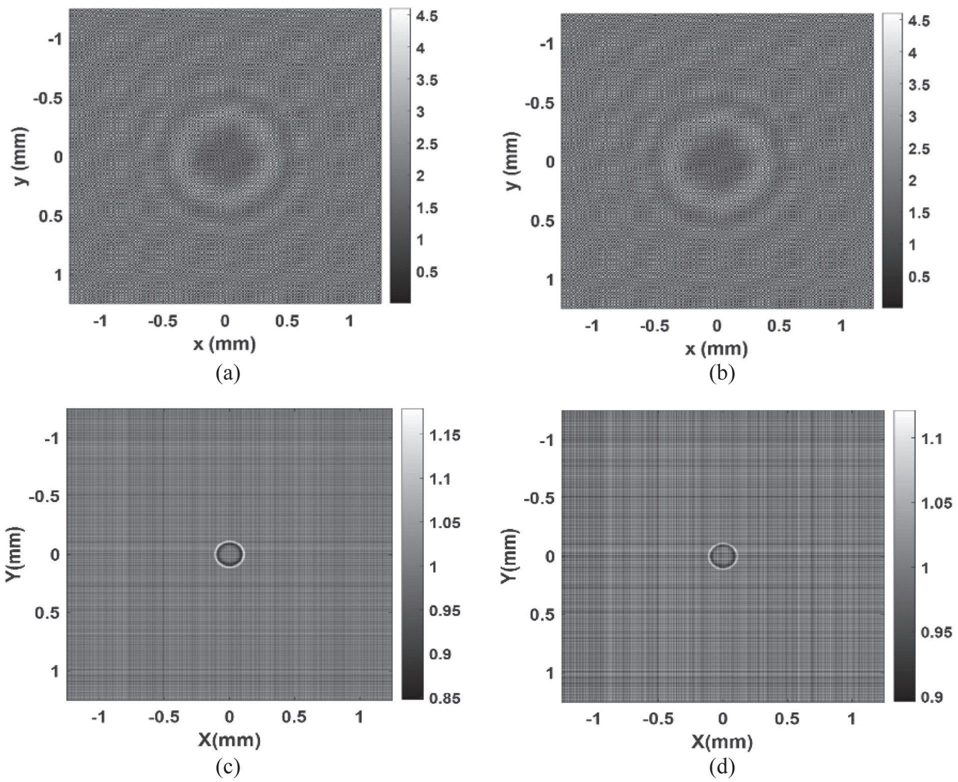

Fig. 18. (a), (b) Two recorded holograms of super-Gaussian phases $V_1 = 3.5$ V and $V_2 = 10$ V giving $\Delta n(V_1) = 0.1838$ and $\Delta n(V_2) = 0.1113$, with the optical path differences corresponding to birefringence being $\mathrm{OPL}(V_1) = 0.00735$ mm and $\mathrm{OPL}(V_2) = 0.00445$ mm, which are reconstructed through back-propagation to the appropriate image plane; (c), (d) intensity profiles $I(x, y; n(V_2))$ and $I(x, y; n(V_1))$ at image (reconstruction through back-propagation) plane for two different voltage values, viz., $V_1 = 3.5$ V and $V_2 = 10$ V.

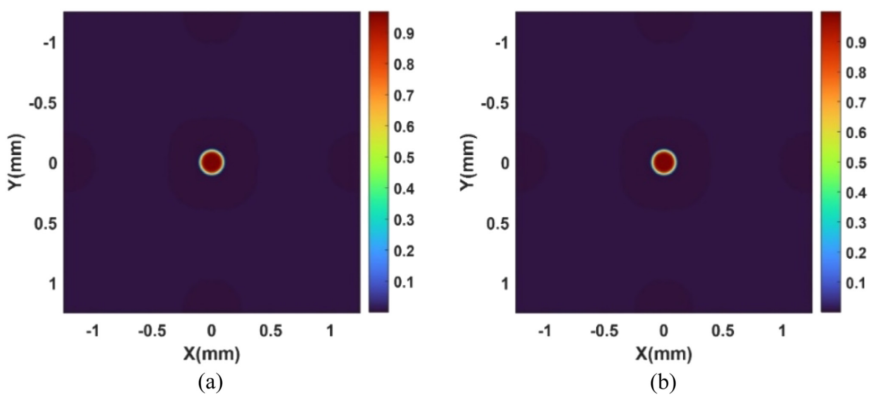

Fig. 19. Super-Gaussian phase retrieval using (a) DH + TIE with LC; (b) DH + TIE + TPE with LC.

Fig. 20(c) shows zoomed-in plots of the wings around the main lobe. The zoomed plots clearly show the differences between the various phase recovery techniques.

Then, the NRMSE is computed using Eq. (20) for each method applied for super-Gaussian phase retrieval and is shown in Table 3 for $m = 5$. As expected, the DH + TIE + TPE with LC performs more accurately than the modified DH + TIE with LC. Once again, the NRMSE values are comparable to those obtained for TIE with LC and TIE + TPE with LC for regular imaging, shown in the earlier example.

6. CONCLUSION

In this paper, we have reviewed TIE and TPE and shown their efficacy when applied to phase retrieval problems involving imaging, either conventional or using DH. More specifically, we have provided verification of the advantage of incorporating the TPE with the TIE in a non-recursive manner for DH-based phase retrieval problems. Using MSE analysis, it was shown that off-axis DH + TIE outperforms SWDH for larger phase excursions while also being computationally less taxing by removing the need for phase unwrapping algorithms. Also shown were the capabilities of DH + TIE, to reduce experimental difficulty and sources of error by retrieving the unwrapped phase of an object

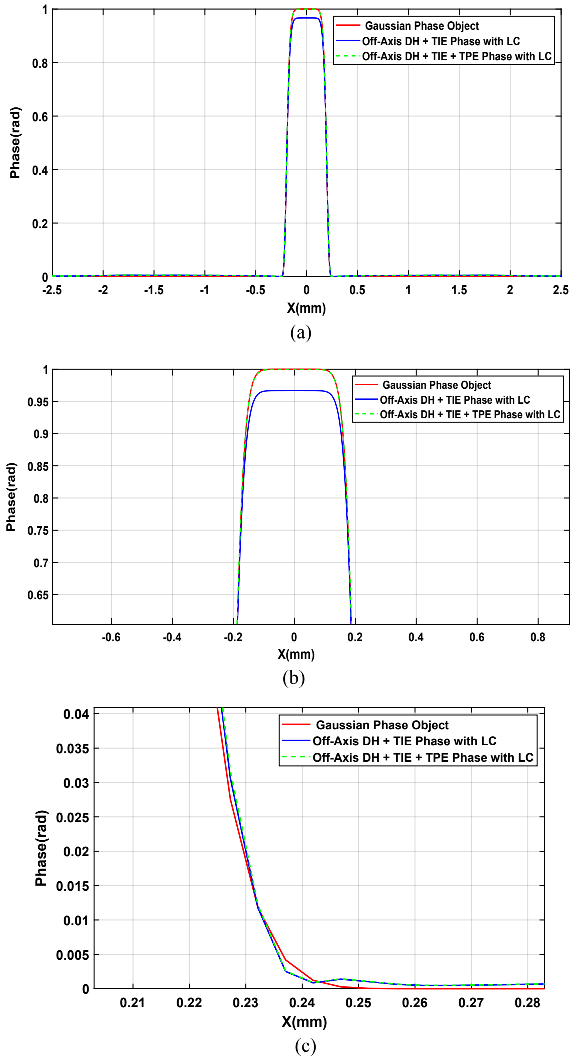

Fig. 20. (a) Cross-sectional profiles of the true phase of the super-Gaussian phase at different values of the powers $m = 5$ (red) and DH + TIE with LC (blue), along with DH + TIE + TPE with LC (dashed green); (b) zoomed-in plots near the super-Gaussian phase peaks; (c) zoomed-in plots of the wings around the main lobe. The zoomed plots clearly show the differences between the various phase recovery techniques.

Table 3. NRMSE Calculations for Super-Gaussian ($m = 5$) Phase Retrieval from Digital Holograms

Method	NRMSE
DH + TIE with LC	0.0353
DH + TIE + TPE with LC	0.0173

without the need for physical displacement of the image sensor or object, as well as reducing the required intensity captures to a single digital hologram.

Ongoing work by our group includes the incorporation of the TPE correction factor to DH + TIE-based phase retrieval and full 3D topogram acquisition of fingermarks coated in CTFs, with emphasis placed on resolving the level-3 details in the fingermark samples. Upon NRMSE analysis, it was conclusively shown that using TIE + TPE with LCs for programmable OPLs in standard-imaging-based phase retrieval and using DH + TIE + TPE with LCs for programmable OPLs in DH-based phase retrieval give better results, respectively, than does TIE with LCs and DH + TIE with LCs. In the latter case, DH + TIE + TPE with LCs provides an approximate 50% reduction in error compared to DH + TIE with LCs. The use of LCs to control the optical path seen by the object beam is quite powerful in that it provides two distinct advantages. First, it removes the need for physical displacement of the image sensor or object when recording multiple intensity images along the propagational axis, thereby reducing errors stemming from imperfect transverse alignment of system components. Second, it allows the capture of many defocused intensity images in very little time via a simple voltage change, which can be used to significantly improve the finite difference derivative estimate and reduce computation time further than employing DH + TIE alone, where numerical propagation to the defocus planes requires discrete Fourier transformations, which is possibly another source of error.

Funding. U.S. Department of Homeland Security (17STCIN00001-05-00); Imam Abdulrahman Bin Faisal University.

Acknowledgment. NAA is sponsored by Imam Abdulrahman Bin Faisal University in Dammam, Saudi Arabia. Her scholarship is administered through the Saudi Cultural Mission (SACM) in the US. Part of the work on digital holography of fingermarks was supported by the US Department of Homeland Security, United States, under Grant Award No. 17STCIN00001-05-00.

Author contributions. The list of author contributions appears below.

Conceptualization: PPB, NAA; *literature review*: AMS, NAA; *experimentation*: NAA, AMS, HAG; *analysis*: NAA; *sample fingermark registration and CTF coating*: MF, AL; *supervision*: PPB; *writing, editing, and review*: NAA, AMS, PPB.

Disclosures. The authors declare no conflicts of interest.

Data availability. Data underlying the results presented in this paper are not publicly available at this time but may be obtained from the authors upon reasonable request.

REFERENCES

1. Y. Shechtman, Y. C. Eldar, O. Cohen, *et al.*, "Phase retrieval with application to optical imaging: a contemporary overview," IEEE Signal Process. Mag. **32**(3), 87–109 (2015).
2. P. Atcheson, S. Acton, and P. Lightsey, "Instrument-level phase retrieval wavefront sensing and correction for astronomical telescopes," Proc. SPIE **4839**, 228–239 (2003).
3. J. R. Fienup and G. B. Feldkamp, "Astronomical imaging by processing Stellar speckle interferometry data," Proc. SPIE **243**, 95–102 (1980).
4. A. J. J. Drenth, A. M. J. Huiser, and H. A. Ferwerda, "The problem of phase retrieval in light and electron microscopy of strong objects," Opt. Acta **22**, 615–628 (1975).
5. R. P. Yu, S. M. Kennedy, D. M. Paganin, *et al.*, "Phase retrieval low energy electron microscopy," Micron **41**, 232–238 (2010).
6. I. K. Robinson, I. A. Vartanyants, G. J. Williams, *et al.*, "Reconstruction of the shapes of gold nanocrystals using coherent x-ray diffraction," Phys. Rev. Lett. **87**, 195505 (2001).
7. R. P. Millane, "Phase retrieval in crystallography and optics," J. Opt. Soc. Am. A **7**, 394–411 (1990).
8. F. Pfeiffer, T. Weitkamp, O. Bunk, *et al.*, "Phase retrieval and differential phase-contrast imaging with low-brilliance x-ray sources," Nat. Phys. **2**, 258–261 (2006).
9. J. Bertolotti, E. G. van Putten, C. Blum, *et al.*, "Non-invasive imaging through opaque scattering layers," Nature **491**, 232–234 (2012).

10. C. L. Curl, C. J. Bellair, P. J. Harris, *et al.*, "Quantitative phase microscopy: a new tool for investigating the structure and function of unstained live cells," Clin. Exp. Pharmacol. Physiol. **31**, 896–901 (2004).
11. A. V. Oppenheim and J. S. Lim, "The importance of phase in signals," Proc. IEEE **69**, 529–550 (1981).
12. F. Zernike, "Phase contrast, a new method for the microscopic observation of transparent objects," Physica **7**, 686–698 (1942).
13. G. Nomarski, "Differential microinterferometer with polarized waves," J. Phys. Radium **16**, 9S–11S (1955).
14. J. W. Goodman and R. W. Lawrence, "Digital image formation from electronically detected holograms," Appl. Phys. Lett. **11**, 77–79 (1967).
15. F. Charriere, J. Kuhn, T. Colomb, *et al.*, "Characterization of microlenses by digital holographic microscopy," Appl. Opt. **45**, 829–835 (2006).
16. Q. Weijuan, C. O. Choo, Y. Yingjie, *et al.*, "Microlens characterization by digital holographic microscopy with physical spherical phase compensation," Appl. Opt. **49**, 6448–6454 (2010).
17. R. Zhou, C. Edwards, G. Popescu, *et al.*, "Semiconductor defect metrology using laser-based quantitative phase imaging," Proc. SPIE **9336**, 93361I (2015).
18. N. Kerwien, A. Tavrov, J. Kaufmann, *et al.*, "Rapid quantitative phase imaging using phase retrieval for optical metrology of phase-shifting masks," Proc. SPIE **5144**, 105–114 (2003).
19. P. Marquet, B. Rappaz, P. J. Magistretti, *et al.*, "Digital holographic microscopy: a noninvasive contrast imaging technique allowing quantitative visualization of living cells with subwavelength axial accuracy," Opt. Lett. **30**, 468–470 (2005).
20. B. Kemper and G. von Bally, "Digital holographic microscopy for live cell applications and technical inspection," Appl. Opt. **47**, A52–A61 (2008).
21. Y. K. Park, C. Depeursinge, and G. Popescu, "Quantitative phase imaging in biomedicine," Nat. Photonics **12**, 578–589 (2018).
22. M. K. Kim, "Principles and techniques of digital holographic microscopy," SPIE Rev. **1**, 018005 (2010).
23. C. Zuo, Q. Chen, W. Qu, *et al.*, "Phase aberration compensation in digital holographic microscopy based on principle component analysis," Opt. Lett. **38**, 1724–1726 (2013).
24. C. Zuo, J. Li, J. Sun, *et al.*, "Transport of intensity equation: a tutorial," Opt. Laser Eng. **135**, 106187 (2020).
25. A. M. Maiden, J. M. Rodenburg, and M. J. Humphry, "Optical ptychography: a practical implementation with useful resolution," Opt. Lett. **35**, 2585–2587 (2010).
26. J. Marrison, L. Raty, P. Marriot, *et al.*, "Ptychography–a label free, high-contrast imaging technique for live cells using quantitative phase information," Sci. Rep. **3**, 2369 (2013).
27. X. Ou, R. Horstmeyer, C. Yang, *et al.*, "Quantitative phase imaging via Fourier ptychographic microscopy," Opt. Lett. **38**, 4845–4848 (2013).
28. G. Nehmetallah and P. Banerjee, "Application of digital and analog holography in three-dimensional imaging," Adv. Opt. Photon. **4**, 472–553 (2012).
29. T.-C. Poon and J.-P. Liu, *Introduction to Modern Digital Holography with MATLAB* (Cambridge, 2014).
30. M. Takeda, H. Ina, and S. Kobayashi, "Fourier-transform method of fringe-pattern analysis for computer-based topography and interferometry," J. Opt. Soc. Am. **72**, 156–160 (1982).
31. T. Kreis, "Application of digital holography for nondestructive testing and metrology: a review," IEEE Trans. Ind. Inf. **12**, 240–247 (2016).
32. Y. Takaki, H. Kawai, and H. Ohzu, "Hybrid holographic microscopy free of conjugate and zero-order images," Appl. Opt. **38**, 4990–4996 (1999).
33. C. J. Mann, L. Yu, C.-M. Lo, *et al.*, "High-resolution quantitative phase-contrast microscopy by digital holography," Opt. Express **13**, 8693–8698 (2005).
34. S. Murata and N. Yasuda, "Potential of digital holography in particle measurement," Opt. Laser Technol. **32**, 567–574 (2000).
35. W. Xu, M. H. Jericho, I. A. Meinertzhagen, *et al.*, "Digital in-line holography for biological applications," Proc. Natl. Acad. Sci. USA **98**, 11301–11305 (2001).
36. A. Alfalou and C. Brosseau, "Optical image compression and encryption methods," Adv. Opt. Photon. **1**, 589–636 (2009).
37. B. Javidi and E. Tajahuerce, "Three-dimensional object recognition by use of digital holography," Opt. Lett. **25**, 610–612 (2000).
38. T. Noda, S. Kawata, and S. Minami, "Three-dimensional phase-contrast imaging by a computed-tomography microscope," Appl. Opt. **31**, 670–674 (1992).
39. J. Gass, A. Dakoff, and M. K. Kim, "Phase imaging without 2π ambiguity by multiwavelength digital holography," Opt. Lett. **28**, 1141–1143 (2003).
40. M. Takeda and M. Kitoh, "Spatiotemporal frequency multiplex heterodyne interferometry," J. Opt. Soc. Am. A **9**, 1607–1614 (1992).
41. P. Clemente, V. Duran, E. Tajahuerce, *et al.*, "Single-pixel digital ghost holography," Phys. Rev. A **86**, 041803 (2012).
42. L. Martinez-Leon, P. Clemente, Y. Mori, *et al.*, "Single-pixel digital holography with phase-encoded illumination," Opt. Express **25**, 4975–4984 (2017).
43. T. Tahara, R. Yonesaka, S. Yamamoto, *et al.*, "High-speed three-dimensional microscope for dynamically moving biological objects based on parallel phase-shifting digital holographic microscopy," IEEE J. Sel. Top. Quantum Electron. **18**, 1387–1393 (2012).
44. I. Yamaguchi and T. Zhang, "Phase-shifting digital holography," Opt. Lett. **22**, 1268–1270 (1997).
45. T. Zhang and I. Yamaguchi, "Three-dimensional microscopy with phase-shifting digital holography," Opt. Lett. **23**, 1221–1223 (1998).
46. P. Guo and A. J. Devaney, "Digital microscopy using phase-shifting digital holography with two reference waves," Opt. Lett. **29**, 857–859 (2004).
47. C.-S. Guo, X. Cheng, X.-Y. Ren, *et al.*, "Optical vortex phase-shifting digital holography," Opt. Express **12**, 5166–5171 (2004).
48. E. Sanchez-Ortiga, A. Doblas, G. Saavedra, *et al.*, "Off-axis digital holographic microscopy: practical design parameters for operating at diffraction limit," Appl. Opt. **53**, 2058–2066 (2014).
49. J. Zhang, S. Dai, C. Ma, *et al.*, "A review of common-path off-axis digital holography: towards high stable optical instrument manufacturing," Light Adv. Manuf. **2**, 333–349 (2021).
50. M. Kumar, O. Matoba, X. Quan, *et al.*, "Single-shot common-path off-axis digital holography: applications in bioimaging and optical metrology [invited]," Appl. Opt. **60**, A195–A204 (2021).
51. O. Matoba, H. Inokuchi, K. Nitta, *et al.*, "Optical voice recorder by off-axis digital holography," Opt. Lett. **39**, 6549–6552 (2014).
52. T. Balciunas, A. Melninkaitis, G. Tamosauskas, *et al.*, "Time-resolved off-axis digital holography for characterization of ultrafast phenomena in water," Opt. Lett. **33**, 58–60 (2008).
53. Y. Emery, T. Colomb, and E. Cuche, "Metrology applications using off-axis digital holography microscopy," J. Phys. Photon. **3**, 034016 (2021).
54. T. Tahara, X. Quan, R. Otani, *et al.*, "Digital holography and its multidimensional imaging applications: a review," Microscopy **67**, 55–67 (2018).
55. J. M. Bioucas-Dias and G. Valadao, "Phase unwrapping via graph cuts," IEEE Trans. Image Process. **16**, 698–709 (2007).
56. J. M. Huntley and H. Saldner, "Temporal phase-unwrapping algorithm for automated interferogram analysis," Appl. Opt. **32**, 3047–3052 (1993).
57. C. F. Lo, X. Peng, and L. Cai, "Surface normal guided method for two-dimensional phase unwrapping," Optik **113**, 439–447 (2002).
58. A. K. Gupta and N. K. Nishchal, "Transport of intensity equation for phase imaging: a review," Asian J. Phys. **28**, 777–786 (2019).
59. M. R. Teague, "Deterministic phase retrieval: a Green's function solution," J. Opt. Soc. Am. **73**, 1434–1441 (1983).
60. N. Streibl, "Phase imaging by the transport equation of intensity," Opt. Commun. **49**, 6–10 (1984).
61. L. Waller, L. Tian, and G. Barbastathis, "Transport of intensity phase-amplitude imaging with higher order intensity derivatives," Opt. Express **18**, 12552–12561 (2010).
62. N. Yoneda, A. Onishi, Y. Saita, *et al.*, "Single-shot higher-order transport-of-intensity quantitative phase imaging based on computer-generated holography," Opt. Express **29**, 4783–4801 (2021).

63. Z. Jingshan, R. A. Claus, J. Dauwels, *et al.*, "Transport of intensity phase imaging by intensity spectrum fitting of exponentially spaced defocus planes," Opt. Express **22**, 10661–10674 (2014).
64. L. Waller, Y. Luo, S. Y. Yang, *et al.*, "Transport of intensity phase imaging in a volume holographic microscope," Opt. Lett. **35**, 2961–2963 (2010).
65. A. K. Gupta, R. Mahendra, and N. K. Nishchal, "Single-shot phase imaging based on transport of intensity equation," Opt. Commun. **477**, 126347 (2020).
66. P. P. Banerjee, A. Korpel, and K. E. Lonngren, "Self-refraction of nonlinear capillary-gravity waves," Phys. Fluids **26**, 2393–2398 (1983).
67. H. Zhou, H. Guo, and P. P. Banerjee, "Non-recursive transport of intensity phase retrieval with the transport of phase," Appl. Opt. **61**, B190–B199 (2022).
68. K. Ichikawa, A. W. Lohmann, and M. Takeda, "Phase retrieval based on the irradiance transport equation and the Fourier transform method: experiments," Appl. Opt. **27**, 3433–3436 (1988).
69. T. E. Gureyev and K. A. Nugent, "Rapid quantitative phase imaging using the transport of intensity equation," Opt. Commun. **133**, 339–346 (1997).
70. D. Paganin and K. A. Nugent, "Noninterferometric phase imaging with partially coherent light," Phys. Rev. Lett. **80**, 2586–2589 (1998).
71. C. Zuo, Q. Chen, and A. Asundi, "Boundary-artifact-free phase retrieval with the transport of intensity equation: fast solution with use of discrete cosine transform," Opt. Express **22**, 9220–9244 (2014).
72. A. Ishizuka, K. Mitsuishi, and K. Ishizuka, "Direct observation of curvature of the wave surface in transmission electron microscope using transport of intensity equation," Ultramicroscopy **194**, 7–14 (2018).
73. E. J. Candes, T. Strohmer, and V. Voroninski, "PhaseLift: exact and stable signal recovery from magnitude measurements via convex programming," arXiv, arXiv:1109.4499v1 (2011).
74. E. J. Candes, Y. C. Eldar, T. Strohmer, *et al.*, "Phase retrieval via matrix completion," SIAM J. Imaging Sci. **6**, 199–225 (2013).
75. R. W. Gerchberg and W. O. Saxton, "A practical algorithm for the determination of phase from image and diffraction plane pictures," Optik **35**, 237–246 (1972).
76. J. R. Fienup, "Reconstruction of an object from the modulus of its Fourier transform," Opt. Lett. **3**, 27–29 (1978).
77. F. Roddier, C. Roddier, and N. Roddier, "Curvature sensing: a new wavefront sensing method," Proc. SPIE **0976**, 203–209 (1988).
78. J. R. Fienup, "Phase retrieval algorithms: a comparison," Appl. Opt. **21**, 2758–2769 (1982).
79. C. Guo, C. Wei, J. Tan, *et al.*, "A review of iterative phase retrieval for measurement and encryption," Opt. Laser Eng. **89**, 2–12 (2017).
80. T. Latychevskaia, "Iterative phase retrieval for digital holography: tutorial," J. Opt. Soc. Am. A **36**, D31–D40 (2019).
81. M. Basunia, P. P. Banerjee, U. Abeywickrema, *et al.*, "Recursive method for phase retrieval using transport of intensity and its applications," Appl. Opt. **55**, 9546–9554 (2016).
82. P. Banerjee, M. Basunia, T.-C. Poon, *et al.*, "An optimized transport-of-intensity solution for phase imaging," Proc. SPIE **9870**, 98700A (2016).
83. H. Zhang, W.-J. Zhou, Y. Liu, *et al.*, "Evaluation of finite difference and FFT-based solutions of the transport of intensity equation," Appl. Opt. **57**, A222–A228 (2018).
84. H. Zhou and P. P. Banerjee, "Transport of intensity phase imaging with error correction using transport of phase equation," Proc. SPIE **11709**, 117090D (2021).
85. A. K. Gupta, A. Fatima, and N. K. Nishchal, "Phase imaging based on transport of intensity equation using liquid crystal variable waveplate," in *Digital Holography and Three-Dimensional Imaging*, OSA Technical Digest (2019), paper M5B.4.
86. A. K. Gupta, A. Fatima, N. K. Nishchal, *et al.*, "Phase imaging based on modified transport of intensity equation using liquid crystal variable retarder with partial coherent illumination," Opt. Rev. **27**, 142–148 (2020).
87. C.-H. Chen, H.-F. Hsu, H.-R. Chen, *et al.*, "Non-interferometric phase retrieval using refractive index manipulation," Sci. Rep. **7**, 46223 (2017).
88. N. Alanazi and P. Banerjee, "Phase imaging using modified transport of intensity and phase equations using electrically controllable optical path lengths," Proc. SPIE **12229**, 1222907 (2022).
89. P. P. Banerjee, "Recent advances in digital holography: referenceless holography using transport of intensity and its applications," in *The International Conference on Fiber Optics and Photonics* (2016), paper W4F.2.
90. U. Abeywickrema, D. Beamer, and P. Banerjee, "Multi-wavelength Fresnel digital holography in an optical system," in *Imaging and Applied Optics Congress* (2016), paper JW4A.57.
91. H. Zhou, M. M. R. Hussain, and P. P. Banerjee, "A review of the dual-wavelength technique for phase imaging and 3D topography," Light Adv. Manuf. **3**, 314–334 (2022).
92. D. P. Kelly, L. Megel, T. Meinecke, *et al.*, "A theoretical comparison of Fresnel based digital holography and phase retrieval from the transport of intensity equation," Proc. SPIE **8833**, 88330G (2013).
93. J. M. Wittkopp, T. C. Khoo, S. Carney, *et al.*, "Comparative phase imaging of live cells by digital holographic microscopy and transport of intensity equation methods," Opt. Express **28**, 6123–6133 (2020).
94. S. Carney, T. C. Khoo, J. Wittkopp, *et al.*, "Digital holographic microscopy (DHM) and transport of intensity (TIE) phase imaging of live cells," Proc. SPIE **11251**, 1125122 (2020).
95. S. Carney, T. C. Khoo, K. Tubbesing, *et al.*, "Quantitative volume comparisons of methamphetamine-induced apoptosis by simultaneous digital holographic microscopy and transport of intensity phase-imaging techniques," Proc. SPIE **11972**, 119720B (2022).
96. J. Tang, J. Zhang, J. Dou, *et al.*, "Comparison of common-path off-axis digital holography and transport of intensity equation in quantitative phase measurement," Opt. Laser Eng. **157**, 107126 (2022).
97. S. Carney, T. C. Khoo, A. Sheikhsofla, *et al.*, "Quantitative phase imaging comparison of digital holographic microscopy and transport of intensity equation phase through simultaneous measurements of live cells," Opt. Laser Eng. **166**, 107581 (2023).
98. C. Zuo, Q. Chen, W. Qu, *et al.*, "Direct continuous phase demodulation in digital holography with use of transport-of-intensity equation," Opt. Commun. **309**, 221–226 (2013).
99. S. Memarzadeh, G. T. Nehmetallah, and P. P. Banerjee, "Noninterferometric tomographic reconstruction of 3D static and dynamic phase and amplitude objects," Proc. SPIE **9117**, 91170M (2014).
100. W. Zhou, S. Liu, C. Wang, *et al.*, "Elimination of quadratic phase aberration in digital holographic microscopy by using transport of intensity," Front. Photon. **3**, 848453 (2022).
101. M. Krenkel, M. Bartels, and T. Salditt, "Transport of intensity phase reconstruction to solve the twin image problem in holographic x-ray imaging," Opt. Express **21**, 2220–2235 (2013).
102. A. Mirando and P. P. Banerjee, "Speckle reduction in phase extracted from off-axis digital holography with transport of intensity," in *Optica Imaging Congress* (2023), paper HM4C.5.
103. Y. Xu, X. Li, Y. Wan, *et al.*, "Multi-particles detection in transformer oil based on lens-free digital holography and transport of intensity equation," Optik **293**, 171399 (2023).
104. A. Mirando and P. Banerjee, "3D polarization imaging by use of digital holography and transport of intensity," Proc. SPIE **12514**, 125140J (2023).
105. W.-J. Zhou, X. Guan, F. Liu, *et al.*, "Phase retrieval based on transport of intensity and digital holography," Appl. Opt. **57**, A229–A235 (2018).
106. H. Zhou, E. Stoykova, and P. P. Banerjee, "Phase retrieval using transport of intensity with off-axis digital holography for objects with large phase excursions," in *OSA Imaging and Applied Optics Congress* (2020), paper HF2D.5.
107. H. Zhou, E. Stoykova, M. Hussain, *et al.*, "Performance analysis of phase retrieval using transport of intensity with digital holography [Invited]," Appl. Opt. **60**, A73–A83 (2021).
108. N. A. Alanazi and P. P. Banerjee, "Phase retrieval using transport of intensity and phase with electrically programmable optical path lengths," in *Digital Holography and 3-D Imaging Optica Technical Digest* (2022), paper Th3A.1.

109. N. A. Alanazi, P. P. Banerjee, M. Faryad, *et al.*, "3D partial bloody fingermark imaging based on digital holography and transport of intensity," in *Optica Imaging Congress* (2023), paper HM2C.4.
110. U. Abeywickrema, P. Banerjee, A. Kota, *et al.*, "High-resolution topograms of fingerprints using multiwavelength digital holography," Opt. Eng. **56**, 034117 (2017).
111. N. Nagachar, T. M. Tiedge, A. Lakhtakia, *et al.*, "Development of environmentally insulted fingermarks on nonporous forensically relevant substrates with conformal columnar thin films," Can. Soc. Forens. Sci. J. **53**, 149–172 (2020).
112. T. M. Tiedge, N. Nagachar, F. R. Wendt, *et al.*, "High-throughput DNA sequencing of environmentally insulted latent fingerprints after visualization with nanoscale columnar-thin-film technique," Sci. Justice **61**, 505–515 (2021).
113. S. F. Williams, D. P. Pulsifer, A. Lakhtakia, *et al.*, "Visualization of partial bloody fingerprints on nonporous substrates using columnar thin films," Can. Soc. Forens. Sci. J. **48**, 20–35 (2015).
114. A. Lakhtakia, R. C. Shaler, R. J. Martín-Palma, *et al.*, "Solid-state acquisition of fingermark topology using dense columnar thin films," J. Forens. Sci. **56**, 612–616 (2011).
115. S. A. Muhlberger, D. P. Pulsifer, A. Lakhtakia, *et al.*, "Optimized development of sebaceous finger marks on nonporous substrates with conformal columnar thin films," J. Forens. Sci. **59**, 94–102 (2014).
116. N. Alanazi, "Phase retrieval and 3D topography using transport of intensity," PhD dissertation (University of Dayton, 2023).
117. N. A. Alanazi and P. P. Banerjee, "Retrieval of phase and 3D topography using modified transport of intensity and phase equations with electrically programmable optical path lengths," Opt. Eng. **62**, 113102 (2023).
118. R. G. Lawandi, K. Hirakawa, and A. M. Sarangan, "Spectroscopy using tunable liquid crystal Fourier filters," Proc. SPIE **11467**, 114670O (2020).
119. S. Huard, *Polarization of Light*, Wiley (1997).
120. V. K. Thakur and M. R. Kessler, eds., *Liquid Crystalline Polymers* (Springer, 2015).
121. Y. H. Lin, H. Ren, and S. T. Wu, "Polarization-independent liquid crystal devices," Liq. Cryst. Today **17**, 2–8 (2008).
122. S. T. Wu, U. Efron, and L. V. D. Hess, "Birefringence measurements of liquid crystals," Appl. Opt. **23**, 3911–3915 (1984).
123. B. Y. Zeldovich and N. V. Tabiryan, "Theory of optically induced Freedericksz transition," Sov. Phys. JETP **55**, 1126–1146 (1982).
124. R. A. Soref and M. J. Rafuse, "Electrically controlled birefringence of thin nematic films," J. Appl. Phys. **43**, 2029–2037 (1972).
125. W. Haase and D. Potzsch, "Light transmission experiments with nematic liquid crystals showing positive and negative dielectric anisotropy," Mol. Cryst. Liq. Cryst. **38**, 77–85 (1977).
126. J. D. Schmidt, *Numerical Simulation of Optical Wave Propagation with Examples in MATLAB* (SPIE, 2010).
127. J. V. Roey, J. V. D. Donk, and P. E. Lagasse, "Beam-propagation method: analysis and assessment," J. Opt. Soc. Am. **71**, 803–810 (1981).
128. M. Mishra and W. P. Hong, "Investigation on propagation characteristics of super-Gaussian beam in highly nonlocal medium," Prog. Electromag. Res. B **31**, 175–188 (2011).
129. S.-H. Bae and M. Kim, "A novel image quality assessment with globally and locally consilient visual quality perception," IEEE Trans. Image Process. **25**, 2392–2406 (2016).